AGU PUBLICATIONS

JGR

Journal of Geophysical Research: Atmospheres

RESEARCH ARTICLE

10.1002/2014JD022968

This article is a companion to *Pavolonis et al.* [2015] doi:10.1002/2014JD022969.

Key Points:
- The Spectrally Enhanced Cloud Objects (SECO) algorithm was developed
- The SECO method can be applied to nearly any satellite sensor
- The SECO approach significantly improves satellite-based ash and dust detection

Supporting Information:
- Table S1

Correspondence to:
M. J. Pavolonis,
Mike.Pavolonis@noaa.gov

Citation:
Pavolonis, M. J., J. Sieglaff, and J. Cintineo (2015), Spectrally Enhanced Cloud Objects—A generalized framework for automated detection of volcanic ash and dust clouds using passive satellite measurements: 1. Multispectral analysis, *J. Geophys. Res. Atmos.*, *120*, 7813–7841, doi:10.1002/2014JD022968.

Received 9 DEC 2014
Accepted 23 MAY 2015
Accepted article online 9 JUN 2015
Published online 11 AUG 2015

The copyright line for this article was changed on 25 SEP 2015 after original online publication.

©2015. The Authors.
This is an open access article under the terms of the Creative Commons Attribution-NonCommercial-NoDerivs License, which permits use and distribution in any medium, provided the original work is properly cited, the use is non-commercial and no modifications or adaptations are made.

Spectrally Enhanced Cloud Objects—A generalized framework for automated detection of volcanic ash and dust clouds using passive satellite measurements: 1. Multispectral analysis

Michael J. Pavolonis[1], Justin Sieglaff[2], and John Cintineo[2]

[1]National Oceanic and Atmospheric Administration Center for Satellite Applications and Research, Madison, Wisconsin, USA, [2]Cooperative Institute for Meteorological Satellite Studies, Madison, Wisconsin, USA

Abstract While satellites are a proven resource for detecting and tracking volcanic ash and dust clouds, existing algorithms for automatically detecting volcanic ash and dust either exhibit poor overall skill or can only be applied to a limited number of sensors and/or geographic regions. As such, existing techniques are not optimized for use in real-time applications like volcanic eruption alerting and data assimilation. In an effort to significantly improve upon existing capabilities, the Spectrally Enhanced Cloud Objects (SECO) algorithm was developed. The SECO algorithm utilizes a combination of radiative transfer theory, a statistical model, and image processing techniques to identify volcanic ash and dust clouds in satellite imagery with a very low false alarm rate. This fully automated technique is globally applicable (day and night) and can be adapted to a wide range of low earth orbit and geostationary satellite sensors or even combinations of satellite sensors. The SECO algorithm consists of four primary components: conversion of satellite measurements into robust spectral metrics, application of a Bayesian method to estimate the probability that a given satellite pixel contains volcanic ash and/or dust, construction of cloud objects, and the selection of cloud objects deemed to have the physical attributes consistent with volcanic ash and/or dust clouds. The first two components of the SECO algorithm are described in this paper, while the final two components are described in a companion paper.

1. Introduction

It is well known that volcanic ash clouds are a major aviation hazard [e.g., *Casadevall*, 1994; *Miller and Casadevall*, 2000; *ICAO*, 2007; *Guffanti et al.*, 2010] and dust clouds play an important, yet not fully understood, role in weather- and climate-scale physical processes in the atmosphere and ocean [e.g., *Dunion and Velden*, 2004; *Evan et al.*, 2011; *Prospero and Lamb*, 2003; *Jickells et al.*, 2005; *Wang et al.*, 2012]. While satellites are a proven resource for detecting and tracking volcanic ash and dust clouds [e.g., *Prata*, 1989a, 1989b; *Wen and Rose*, 1994; *Ackerman*, 1997; *Schneider et al.*, 1999; *Prata and Grant*, 2001; *Rose et al.*, 2000; *Legrand et al.*, 2001; *Darmenov and Sokolik*, 2005; *Pavolonis et al.*, 2006; *Evan et al.*, 2006; *DeSouza-Machado et al.*, 2010; *Corradini et al.*, 2010; *Prata and Prata*, 2012; *Francis et al.*, 2012; *Pavolonis et al.*, 2013; *Clarisse et al.*, 2013], existing methods, while all valuable, have several important limitations that served as the motivation to develop a new approach. In particular, existing satellite-based methodologies have one or more of the following limitations.

1. The end results are qualitative and hence require manual interpretation and, as such, cannot be used in quantitative applications [e.g., *Hillger and Clark*, 2002a, 2002b; *Ellrod et al.*, 2003; *Miller*, 2003; *Lensky and Rosenfeld*, 2008].
2. The results depend strongly on solar zenith angle, and/or the technique is only applicable over a subset of solar zenith angles [e.g., *Legrand et al.*, 2001; *de Graaf et al.*, 2005; *Pavolonis et al.*, 2006; *Evan et al.*, 2006; *Scollo et al.*, 2012].
3. The technique can only be applied to a specific instrument or a small subset of instruments [e.g., *Liu et al.*, 2008; *Clarisse et al.*, 2010; *DeSouza-Machado et al.*, 2010; *Gangale et al.*, 2010; *Winker et al.*, 2012; *Clarisse et al.*, 2013] and hence does not provide frequent (<60 min) global coverage.
4. Finally, no published technique capable of providing frequent global coverage has been shown to be consistently skillful (very high probability of detection and very low false alarm rate) over a large range

of cloud properties (cloud height/temperature/pressure, geometric thickness, composition, particle size, and cloud optical depth) and background states (surface emissivity, surface temperature, atmospheric temperature, and atmospheric composition).

Given the above limitations, existing satellite-based ash/dust detection techniques are not optimized for many important practical (operational) and research applications. For instance, Volcanic Ash Advisory Centers, which are responsible for operationally issuing volcanic ash advisories to the aviation community, currently heavily rely on manual analysis of satellite imagery to track volcanic ash clouds. It is not feasible to routinely manually examine every satellite image for volcanic ash clouds, so some volcanic ash clouds go undetected for several hours [e.g., *Pavolonis et al*., 2006]. Thus, a reliable, fully automated, satellite-based volcanic ash detection system is needed to help improve the timeliness of volcanic ash advisories. The retrieval of important volcanic ash cloud properties such as cloud height, mass loading, and effective radius requires a priori knowledge of the horizontal location of ash to constrain the inversion problem and prevent false alarms (pixels with valid retrieval results that are outside of the ash cloud(s)) without significantly decreasing the probability of detection [e.g., *Prata and Prata*, 2012; *Francis et al*., 2012; *Pavolonis et al*., 2013]. Operational forecasters generally rely on manually initiated model simulations that utilize eruption source parameters that are prone to large errors, especially outside of the coverage of cloud or precipitation radars [*Arason et al*., 2011; *Schneider and Hoblitt*, 2013].

While many satellite-based dust detection algorithms exist [e.g., *Peyridieu et al*., 2013; *Ashpole and Washington*, 2012; *Hsu et al*., 2013; *Remer et al*., 2013; *Tanre et al*., 2011; *Clarisse et al*., 2013; *Diner et al*., 2001; *Hong*, 2009; *Evan et al*., 2006], a generalized approach, analogous to the generalized approach developed for hyperspectral infrared data by *Clarisse et al*. [2013], that can be applied to nearly any narrow or broadband geostationary or low earth orbit sensor, day or night, over land or over water, does not exist. Such an approach can complement existing dust detection approaches for practical and research applications.

In an effort to address all of the aforementioned limitations of previously published volcanic ash and dust detection methods, the Spectrally Enhanced Cloud Objects (SECO) technique has been developed. The SECO algorithm utilizes a combination of radiative transfer theory, a statistical model, and image processing techniques to identify volcanic ash and dust clouds in satellite imagery with skill comparable to that of a human expert. The fully automated SECO technique is globally applicable and can be adapted to a wide range of low earth orbit and geostationary satellite sensors. Combinations of satellite sensors can even be used to further increase the skill. The SECO algorithm is designed to take full advantage of each sensor's volcanic ash/dust-relevant capabilities. The SECO algorithm is described in a two-part paper series. Part I (this paper) will describe how the SECO algorithm utilizes advanced multispectral metrics to identify satellite pixels that potentially contain volcanic ash and/or dust with improved skill relative to the most utilized existing method. In Part 2 [*Pavolonis et al.,* 2015], the cloud object-based techniques that are applied to the results of the multispectral analysis, described in this paper, will be discussed. In addition, *Pavolonis et al.* [2015] demonstrate that the end results of the complete SECO algorithm are comparable to manual analysis performed by human experts. The SECO technique is the first fully automated algorithm, applicable to nearly any satellite sensor with infrared capabilities, which can be used in advanced real-time applications such as ash cloud alerting and ash/dust cloud dispersion forecasting. The SECO technique can also serve as a valuable research tool.

2. Satellite Measurements

The SECO method is designed such that it can be applied to nearly any low earth orbit or geostationary (GEO) imaging sensor, such that frequent global results can be obtained. The method can also be applied to sounding instruments, including hyperspectral infrared sounders, but this paper will focus on the higher spatial resolution (and higher temporal resolution in the case of GEO) measurements offered by imaging instruments. Spectral measurements centered near 0.65 (daytime only), 3.9, 7.3, 8.5, 11, and 12 μm can be used by the SECO algorithm. The rationale for selecting these channels will be described in a later section. More specifically, the SECO algorithm can utilize any of the channel combinations shown in Table 1. For each channel combination, some of the relevant sensors are also listed (Table 2 defines the sensor

Table 1. Possible Spectral Channel Combinations That can be Used in the Ash/Dust Detection Algorithm are Shown as a Function of Satellite Imaging Sensor Spectral Capabilities (Relevant to Ash and Dust Detection)[a]

Approximate Central Wavelength	Sensor Channel Numbers	Conditions Required for Use[b]
Tier I Sensors: MODIS, MSG SEVIRI, GOES-R ABI, Himawari-8/9 AHI, MTG FCI		
0.65, 3.9, 7.3, 8.5, 11, 12 μm	1, 20, 28, 29, 31, 32 1, 4, 6, 7, 9, 10 2, 7, 10, 11, 14, 15 3, 7, 10, 11, 14, 15 3, 9, 11, 12, 14, 15	Solar zenith angle < 85° and no sun glint
3.9, 7.3, 8.5, 11, 12 μm	20, 28, 29, 31, 32 4, 6, 7, 9, 10 7, 10, 11, 14, 15 7, 10, 11, 14, 15 9, 11, 12, 14, 15	Solar zenith angle > 90° and no detectable stray light
7.3, 8.5, 11, 12 μm	28, 29, 31, 32 6, 7, 9, 10 10, 11, 14, 15 10, 11, 14, 15 11, 12, 14, 15	Only used if previous two channel combinations are not possible
8.5, 11, 12 μm	29, 31, 32 7, 9, 10 11, 14, 15 11, 14, 15 12, 14, 15	Only used if previous three channel combinations are not possible
11, 12 μm	31, 32 9, 10 14, 15 14, 15 14, 15	Only used if previous four channel combinations are not possible
Tier II Sensors: VIIRS		
0.65, 3.9, 8.5, 11, 12 μm	M5, M12, M14, M15, M16	Solar zenith angle < 85° and no sun glint
3.9, 8.5, 11, 12 μm	M12, M14, M15, M16	Solar zenith angle > 90° and no detectable stray light
8.5, 11, 12 μm	M14, M15, M16	Only used if previous two channel combinations are not possible
11, 12 μm	M15, M16	Only used if previous three channel combinations are not possible
Tier III Sensors: AVHRR, COMS-MI, GOES Imager,[c] MTSAT Imager		
0.65, 3.9, 11, 12 μm	1, 3b, 4, 5 1, 2, 4, 5 1, 2, 4, 5 1, 5, 2, 3	Solar zenith angle < 85° and no sun glint
3.9, 11, 12 μm	3b, 4, 5 2, 4, 5 2, 4, 5 5, 2, 3	Solar zenith angle > 90° and no detectable stray light
11, 12 μm	4, 5 4, 5 4, 5 2, 3	Only used if previous two channel combinations are not possible

[a]Tier I sensors offer the most channels of relevance to the ash/dust detection algorithm presented in this paper, and Tier III sensors offer the least. Sun glint is assumed to be present over water surfaces if the glint angle is less than 40°. Stray light is assumed to be present if the solar zenith angle exceeds 90° and the measured 0.65 μm count is greater than a sensor-dependent threshold. Please see Table 2 for a list of sensor acronyms.

[b]Each channel in a given spectral combination must also pass quality control. If one or more channels in a combination does not pass quality control, the next best channel combination is attempted.

[c]The 12 μm channel is only available on the GOES 8–11 spacecraft.

Table 2. The Satellite Imaging Radiometers of Greatest Relevance to the Ash/Dust Detection Algorithm Described in This Paper Are Listed Below[a]

Sensor Acronym	Acronym Meaning
AVHRR	Advanced Very High Resolution Radiometer
COMS-MI	Communication, Ocean, and Meteorological Satellite (COMS) Meteorological Imager (MI)
GOES Imager	Geostationary Operational Environmental Satellite (GOES) Imager
GOES-R ABI[b]	Next Generation Geostationary Operational Environmental Satellite (GOES-R) Advanced Baseline Imager (ABI)
Himawari-8/9 AHI[b]	Himawari-8/9 Advanced Himawari Imager (AHI)
MODIS	Moderate Resolution Imaging Spectroradiometer
MTSAT Imager	Multifunctional Transport Satellites (MTSAT) Imager
MSG SEVIRI	Meteosat Second Generation (MSG) Spinning Enhanced Visible and Infrared Imager
MTG FCI[b]	Meteosat Third Generation (MTG) Flexible Combined Imager (FCI)
VIIRS	Visible Infrared Imaging Radiometer Suite

[a]Each sensor may be present on multiple spacecraft with different orbital parameters.
[b]Capability will be launched and deployed in 2014 or later.

acronyms). The algorithm is designed to utilize the greatest number of spectral channels possible for a given sensor, taking into account the quality of each spectral measurement on a pixel-by-pixel basis. While measurements that directly depend on solar zenith angle are utilized when possible, the SECO approach does not require sunlight to be present. The algorithm can operate solely with measurements that are not influenced by reflected sunlight. This approach can be applied to hyperspectral infrared data by selecting micro windows [e.g., *Turner*, 2005] that sample the same spectral regions listed in Table 1 or, perhaps, through the use of absorption optical depth spectra that can be used to compute slopes in cloud optical depth as a function of wavenumber [see *Pavolonis*, 2010, Figure 2].

The Moderate Resolution Imaging Spectroradiometer (MODIS), which has all the spectral channels (with a 1 km resolution at nadir) required to test each possible channel combination, is the primary instrument for developing and demonstrating the SECO approach. In Part 2 of this paper [*Pavolonis et al.,* 2015], results from other sensors will also be briefly highlighted to help illustrate that the SECO approach is generic and robust enough to be applied to virtually any sensor (past, current, and future sensors included). The operational meteorological imaging sensor (as of early 2014) excluded from Tables 1 and 2 is the Geostationary Operational Environmental Satellite (GOES) Imager on GOES 12–15 [*Schmit et al*., 2001]. The 12 μm channel on GOES 12–15 was replaced by a 13.3 μm channel, which, due to CO_2 absorption, is more challenging to use for detecting volcanic ash and dust [*Ellrod*, 2004]. We have developed the ability to utilize the 13.3 μm channel in lieu of the 12 μm channel, but this will not be discussed in this paper in order to focus on the more common case of the 12 μm channel being available.

3. Definition of Volcanic Ash and Dust Clouds

Prior to describing the SECO algorithm, we must first explain how we define volcanic ash and dust clouds. In this paper, volcanic ash and dust clouds are defined as a collection of satellite pixels that can be manually identified as ash or dust in well-scaled multispectral (visible, near-infrared, and infrared) *passive* satellite imagery by a human expert. Such a definition is quite reasonable given that automated algorithms can only detect volcanic ash or dust if a spatially and temporally (if applicable) coherent signature is present in the calibrated radiances for a given satellite sensor (e.g., the ash or dust cloud contributes to the measured spectral radiances more than noise). Thus, there are two general scenarios in which airborne ash or dust, if actually present, cannot be qualitatively (and hence quantitatively) detected using passive satellite data: (1) overlapping cloud layers obscure the ash or dust cloud, (2) the mass loading of the ash is below detection limits for a given set of observing conditions and instrument capabilities. *Prata and Prata* [2012], *Francis et al.* [2012], and *Pavolonis et al*. [2013] showed that volcanic ash can generally be identified in passive satellite observations if it is the highest cloud layer and has a concentration with an order of magnitude of 10^{-2} g/m^2 or greater. Multispectral false color imagery sometimes referred to as red-green-blue or RGB imagery is a proven tool used by human analysts, including operational forecasters, to manually identify volcanic ash and dust [*Lensky and Rosenfeld*, 2008; *Millington et al*., 2012]. Volcanic ash- and dust-relevant false color imagery is designed to maximize the color contrast (subject to color vision limitations and differences) between

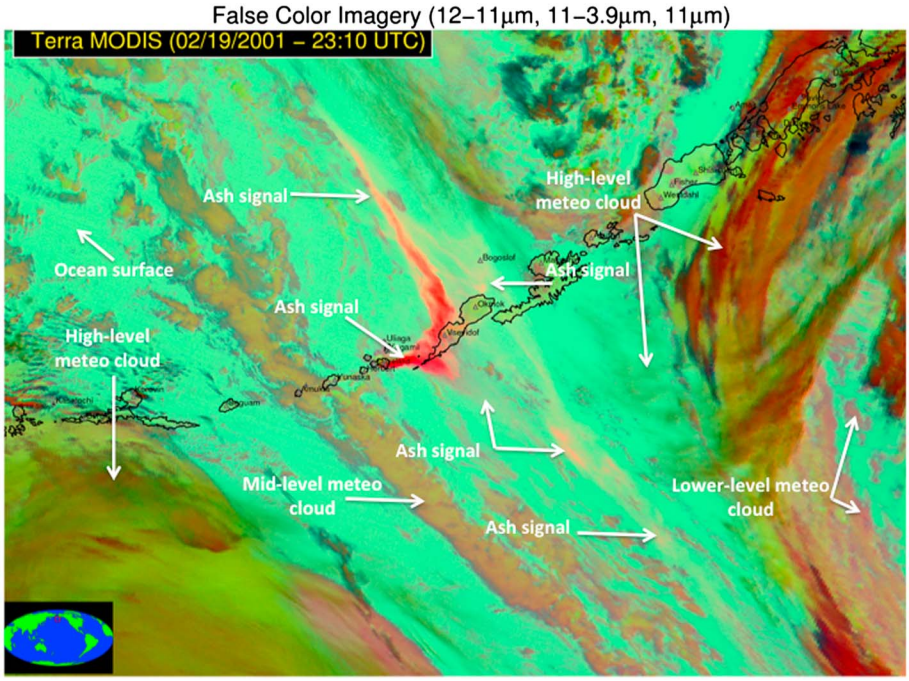

Figure 1. A false color *Terra* MODIS image centered on the Aleutian Islands (Alaska) on 19 February 2001 at 23:10 UTC is shown. The 12–11 μm brightness temperature difference (BTD) is displayed on the red color gun, the 11–3.75 μm BTD is displayed on the green color gun, and the 11 μm brightness temperature is displayed on the blue color gun. The white annotations are used to highlight some important features. The volcanic ash cloud was produced by an eruption of Mount Cleveland, Alaska. In the annotations, "meteo cloud" refers to liquid water or ice clouds generated by typical meteorological processes. This MODIS image was taken from the sunlit portion of the orbit.

volcanic ash and dust and all other observable features (other cloud types and clear-sky features) by exploiting the unique spectral variability of absorption and reflection exhibited by volcanic ash and dust relative to other cloud types and most surface features. More specifically, well-known absorption and reflection properties at wavelengths centered near 3.9, 8.5, 11, and 12 μm are exploited [*Prata and Grant*, 2001; *Pavolonis et al*., 2006; *Lensky and Rosenfeld*, 2008; *Pavolonis*, 2010; *Francis et al*., 2012; *Pavolonis et al*., 2013]. Examples of false color imagery with a volcanic ash cloud are shown in Figures 1 and 2, and the corresponding 11–12 μm "split-window" brightness temperature difference (BTD) is shown in Figure 3. A detailed description of the RGB imagery utilized in this paper is given by *Pavolonis* [2014].

4. SECO Algorithm—Multispectral Analysis

The SECO algorithm is comprised of four primary components. First, calibrated and navigated spectral measurements are converted to more robust spectral parameters when possible (e.g., increased sensitivity to cloud composition and decreased sensitivity to background conditions). Next, the spectrally robust multispectral metrics and a naïve Bayesian approach are used to estimate the probability that a given satellite pixel is part of an ash or dust cloud. In the third component of the SECO algorithm, spatially connected satellite pixels that exceed an ash/dust probability threshold are grouped into cloud objects and various statistical properties are computed for each cloud object. Finally, the cloud object statistics are used to determine which objects are most likely ash/dust clouds. All pixels associated with objects determined to be volcanic ash or dust are classified as ash/dust and all other pixels are classified as a nonash/nondust feature. The first two components of the SECO algorithm (derivation of advanced multispectral metrics and estimation of ash/dust probability) are described in the following sections of this paper, while the cloud object components are described in Part 2 [*Pavolonis et al.,* 2015].

4.1. Description of Spectral Metrics

Most of the infrared-based spectral metrics are based on *Pavolonis* [2010] and *Pavolonis et al*. [2013]. In lieu of infrared brightness temperatures and brightness temperature differences, which are very sensitive to

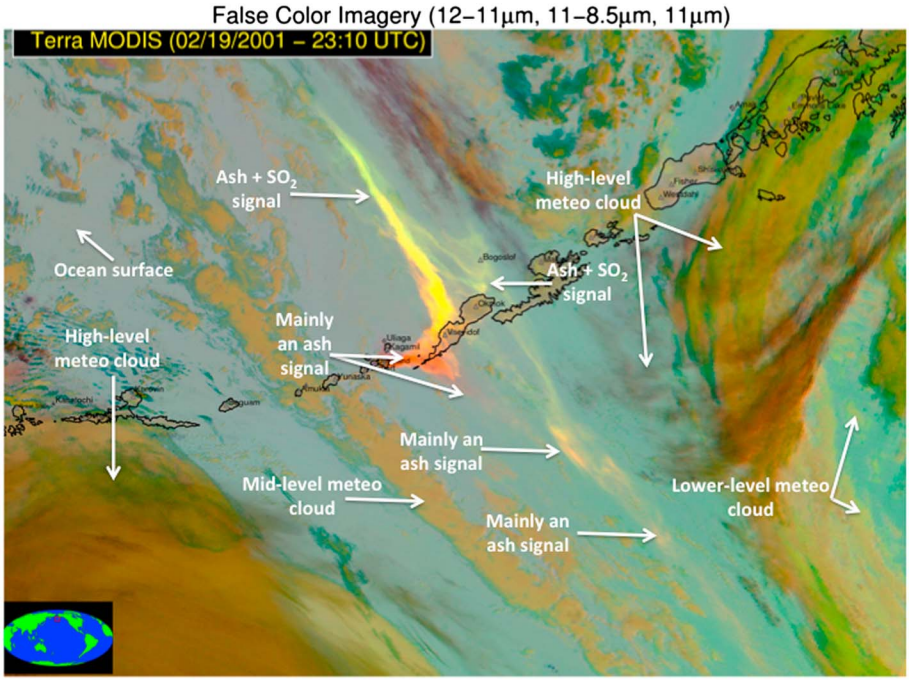

Figure 2. Same as Figure 1 except that the 12–11 μm brightness temperature difference (BTD) is displayed on the red color gun, the 11–8.5 μm BTD is displayed on the green color gun, and the 11 μm brightness temperature is displayed on the blue color gun.

background conditions (surface temperature, surface emissivity, atmospheric moisture, and temperature), cloud emissivity and radiative parameters known as β ratios are utilized. As demonstrated by *Heidinger and Pavolonis* [2009], *Pavolonis* [2010], and *Pavolonis et al.* [2013], the effective cloud emissivity at a given infrared wavelength is computed as given in equations (1) and (2).

$$\varepsilon_{\mathrm{eff}}(\lambda) = \frac{R_{\mathrm{obs}}(\lambda) - R_{\mathrm{clr}}(\lambda)}{R_{\mathrm{cld}}(\lambda) - R_{\mathrm{clr}}(\lambda)} \tag{1}$$

$$R_{\mathrm{cld}}(\lambda) = B(\lambda, T_{\mathrm{eff}})t_{\mathrm{ac}}(\lambda) + R_{\mathrm{ac}}(\lambda) \tag{2}$$

In equation (1), which is derived by *Pavolonis* [2010] in Appendix A, λ is the wavelength, R_{obs} is the observed radiance, R_{clr} is the clear-sky radiance, and R_{cld} is the blackbody emission from the cloud that is transmitted to the top of the atmosphere. The effective cloud emissivity [*Cox*, 1976] is denoted by $\varepsilon_{\mathrm{eff}}$. The effects of cloud scattering are implicitly captured by the effective cloud emissivity [see *Cox*, 1976]. In equation (2), R_{ac} and t_{ac} are the above-cloud upwelling atmospheric radiance and transmittance, respectively. B is the Planck function, and T_{eff} is the effective cloud temperature. The effective cloud temperature is most often different from the thermodynamic cloud top temperature since the emission of radiation originates from a layer in the cloud. The depth of this layer depends on the cloud extinction profile, which is generally unknown. The clear-sky transmittance and radiance terms are determined using surface temperature, atmospheric temperature, water vapor, and ozone profiles from the Global Forecast Model (GFS) [*Hamill et al.*, 2006], surface emissivity from the SeeBor database [*Seemann et al.*, 2008], the satellite zenith angle, and a regression-based clear-sky radiative transfer model [*Hannon et al.*, 1996]. The procedure for determining the clear-sky radiance and transmittance is the same as described by *Heidinger and Pavolonis* [2009], *Heidinger et al.* [2010], and *Pavolonis* [2010]. In addition, a discussion on the impacts of errors in the GFS fields is discussed in section 4.2 and in Part 2 of this manuscript [*Pavolonis et al.,* 2015].

The spectral variation of the effective cloud emissivity is directly related to cloud microphysical information (e.g., particle size, shape, composition, etc.). Effective optical depth ratios, otherwise known as β ratios, have been previously used to extract cloud microphysical information from infrared measurements [*Inoue*, 1985, 1987; *Parol et al.*, 1991; *Giraud et al.*, 1997; *Heidinger and Pavolonis*, 2009; *Pavolonis*, 2010; *Pavolonis et al.*, 2013]. For a given

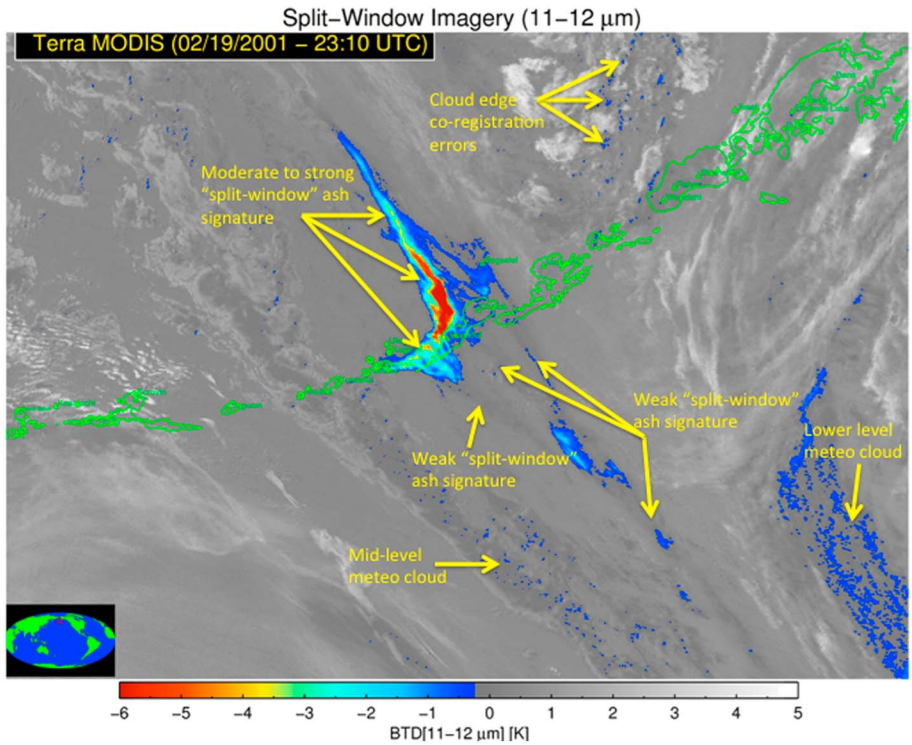

Figure 3. Same as Figure 1 except the 11–12 μm "split-window" brightness temperature difference is shown.

spectral pair of effective emissivity ($\varepsilon_{\mathrm{eff}}(\lambda_1)$ and $\varepsilon_{\mathrm{eff}}(\lambda_2)$) or effective absorption optical depth ($\tau_{\mathrm{abs,eff}}(\lambda_1)$ and $\tau_{\mathrm{abs,eff}}(\lambda_2)$), the effective absorption optical depth ratio, $\beta(\lambda_1, \lambda_2)$, can be computed using equation (3).

$$\beta(\lambda_1, \lambda_2) = \frac{\ln[1 - \varepsilon_{\mathrm{eff}}(\lambda_1)]}{\ln[1 - \varepsilon_{\mathrm{eff}}(\lambda_2)]} = \frac{\tau_{\mathrm{abs,eff}}(\lambda_1)}{\tau_{\mathrm{abs,eff}}(\lambda_2)} \tag{3}$$

In order to compute $\beta(\lambda_1, \lambda_2)$ for a given spectral pair, the location of the radiative center of the cloud, in the vertical, must be specified (see equations (1) and (2)) but is unknown since pixels that likely contain ash or dust must be identified prior to retrieving cloud properties such as T_{eff} [*Pavolonis et al.*, 2013]. Thus, the "top of troposphere" and "opaque cloud" assumptions, described in detail by *Pavolonis* [2010], are utilized. The "top of troposphere" β ratio, $\beta_{\mathrm{tot}}(\lambda_1, \lambda_2)$, is computed by assuming that the cloud radiative center is located at the top of the troposphere. The "opaque cloud" β ratio, $\beta_{\mathrm{opaque}}(\lambda_1, \lambda_2)$, is computed by assuming that the cloud radiative center is located at the highest level of the troposphere that results in $\varepsilon_{\mathrm{eff}}(\lambda_1)$ or $\varepsilon_{\mathrm{eff}}(\lambda_2)$ being equal to 0.98 (using equation (1)). As described by *Pavolonis* [2010], the "top of troposphere" assumption is very effective for determining the composition of semitransparent clouds, while the "opaque cloud" assumption provides some additional skill, particularly when classifying optically thick clouds. $\beta_{\mathrm{tot}}(\lambda_1, \lambda_2)$ and $\beta_{\mathrm{opaque}}(\lambda_1, \lambda_2)$, while very useful, do not account for underlying cloud layers. Semitransparent ash and dust clouds will often reside above one or more meteorological cloud layers. In an attempt to roughly account for the influence of an underlying liquid water or ice cloud layer, a second set and a third set of "top of troposphere" β ratios are computed (only for 11 and 12 μm spectral pairing) by replacing $R_{\mathrm{clr}}(\lambda)$ in equation (1) with the top of atmosphere radiance produced by a blackbody emitter located at the 0.8 and 0.7 sigma levels (a terrain following vertical coordinate), respectively. The pressure level (P) associated with a given sigma (σ) value is computed using equation (4).

$$P = (P_{\mathrm{surface}})\sigma \tag{4}$$

The 0.8 sigma level is used to approximate a low-level (relative to the surface) underlying cloud layer, and $\sigma = 0.7$ is used to approximate a midlevel underlying cloud layer. The second set of β ratios is denoted by $\beta_{\mathrm{tot_\sigma 8}}(\lambda_1, \lambda_2)$, and the third set is denoted by $\beta_{\mathrm{tot_\sigma 7}}(\lambda_1, \lambda_2)$.

The choice of spectral channel pairings (λ_1, λ_2) used to construct β ratios is designed to take advantage of absorption/scattering features that are generally unique to volcanic ash and/or dust clouds. As shown by *Pavolonis* [2010] and *Pavolonis et al*. [2013], the combination of β(12 μm, 11 μm) and β(8.5 μm, 11 μm) is extremely useful for discriminating between volcanic ash/dust clouds and other cloud features. In the absence of large amounts of SO_2, β(8.5 μm, 11 μm) and, to a lesser extent, β(12 μm, 11 μm) can individually take on similar values as meteorological clouds. The combination of β(12 μm, 11 μm) and β(8.5 μm, 11 μm), however, is less likely to spectrally overlap with meteorological clouds [see *Pavolonis et al*., 2013, Figure 4]. When larger amounts (>5 Dobson units) of SO_2 are present, as is common in clouds produced by volcanic eruptions, β(8.5 μm, 11 μm) takes on large values that are generally outside of the normal range for meteorological clouds, while β(12 μm, 11 μm) is not impacted by SO_2. Thus, even if SO_2 is present in or above the ash cloud, the combination β(12 μm, 11 μm) and β(8.5 μm, 11 μm) still exhibits behavior that is generally unique to volcanic ash clouds.

Figures 4 and 5 show the β_{tot}(12 μm, 11 μm), β_{opaque}(12 μm, 11 μm), $\beta_{tot_\sigma 8}$(12 μm, 11 μm), $\beta_{tot_\sigma 7}$(12 μm, 11 μm), β_{tot}(8.5 μm, 11 μm), and β_{opaque}(8.5 μm, 11 μm) parameters computed for the scenes introduced in section 3. When $\varepsilon(\lambda_1)$ and/or $\varepsilon(\lambda_2)$ is less than zero, the 11 μm brightness temperature is imaged in Figures 4 and 5. Note how β_{tot}(8.5 μm, 11 μm) (Figures 4f and 5f) and β_{opaque}(8.5 μm, 11 μm) (Figures 4g and 5g) are much larger in regions with ash plus significant SO_2 compared to ash regions that are not coupled with a significant SO_2 spectral signature. The spatial variability of β_{tot}(12 μm, 11 μm) (Figures 4b and 5b), β_{opaque}(12 μm, 11 μm) (Figures 4c and 5c), $\beta_{tot_\sigma 8}$(12 μm, 11 μm) (Figures 4d and 5d), and $\beta_{tot_\sigma 7}$(12 μm, 11 μm) (Figures 4e and 5e) within the volcanic cloud can be generally attributed to varying cloud microphysical properties, especially the effective particle radius [*Pavolonis et al*., 2013]. The majority of the volcanic ash in Figures 4 and 5 does not overlap lower cloud layers, so $\beta_{tot_\sigma 8}$(12 μm, 11 μm) (Figures 4d and 5d) and $\beta_{tot_\sigma 7}$(12 μm, 11 μm) (Figures 4e and 5e) most often do not have valid values. In regions where a valid multilayer version of β(12 μm, 11 μm) cannot be computed, the 11 μm brightness temperature is displayed, revealing that the majority of the ash cloud in both scenes is optically thin (very weak presentation in 11 μm image as inferred by relatively high brightness temperatures compared to other portions of the ash cloud).

The combination of β(12 μm, 11 μm) and β(7.3 μm, 11 μm) is also exploited as it aids in the detection of high-level volcanic ash and dust (dust, in large quantities, is less likely to be present at high levels than volcanic ash). The 7.3 μm channel is centered on a fairly strong water vapor absorption feature, so the clear-sky weighting function peaks in the middle troposphere in all but the driest of atmospheres. Thus, β(7.3 μm, 11 μm) is only useful when midlevel to high-level clouds is present. In the absence of SO_2 (strong SO_2 absorption features are captured by the 7.3 μm channel), the increase in cloud absorption as a function of increasing wavelength between 7.3 and 11 μm is much greater for volcanic ash and dust than liquid water or ice clouds, resulting in midlevel and high-level ash and dust clouds generally taking on smaller values of β(7.3 μm, 11 μm) compared to meteorological clouds [see *Pavolonis*, 2010, Figure 1]. When midlevel to high-level SO_2 is present, β(7.3 μm, 11 μm) will be very large such that it is out of the normal range that encompasses meteorological clouds, making it particularly useful for volcanic ash detection.

It is important to note that SO_2 absorption at 11 and 12 μm is negligible, so a β(12 μm, 11 μm) signal consistent with ash must always be present regardless of the influence of SO_2 absorption, since β(7.3 μm, 11 μm) and β(8.5 μm, 11 μm) are always used in tandem with β(12 μm, 11 μm). The β_{tot}(7.3 μm, 11 μm) parameter is shown in Figures 4h and 5h. The SO_2 sensitivity is clearly discernable by the large β_{tot}(7.3 μm, 11 μm) values in regions where a strong SO_2 spectral signature is present. The 12–11, 11–8.5, and 11 μm false color image from 19 February 2001 (23:10 UTC) (Figures 2 and 4) indicates that the region of ash near Cleveland volcano does not have a strong SO_2 spectral signature like many other portions of the ash cloud at this time. The lack of an obvious SO_2 spectral signature in the 12–11, 11–8.5, 11 μm false color image is supported by collocated β_{tot}(7.3 μm, 11 μm) values that are small, as would be expected for volcanic ash in the absence of significant SO_2. As shown by *Watson et al*. [2004], H_2SO_4 aerosol absorbs and scatters radiation across the spectrum from 7 to 13 μm. The spectral variability of the total attenuation (numerical range of the transmittance) is small *relative* to that of ash and, especially, SO_2. Thus, β(7.3 μm, 11 μm) is far more sensitive to SO_2 than H_2SO_4. As shown by *Prata* [1989a] and *Watson et al*. [2004], H_2SO_4 can produce a signal in the 11–12 μm window that is similar to ash. As a result, our approach is susceptible to overestimating the

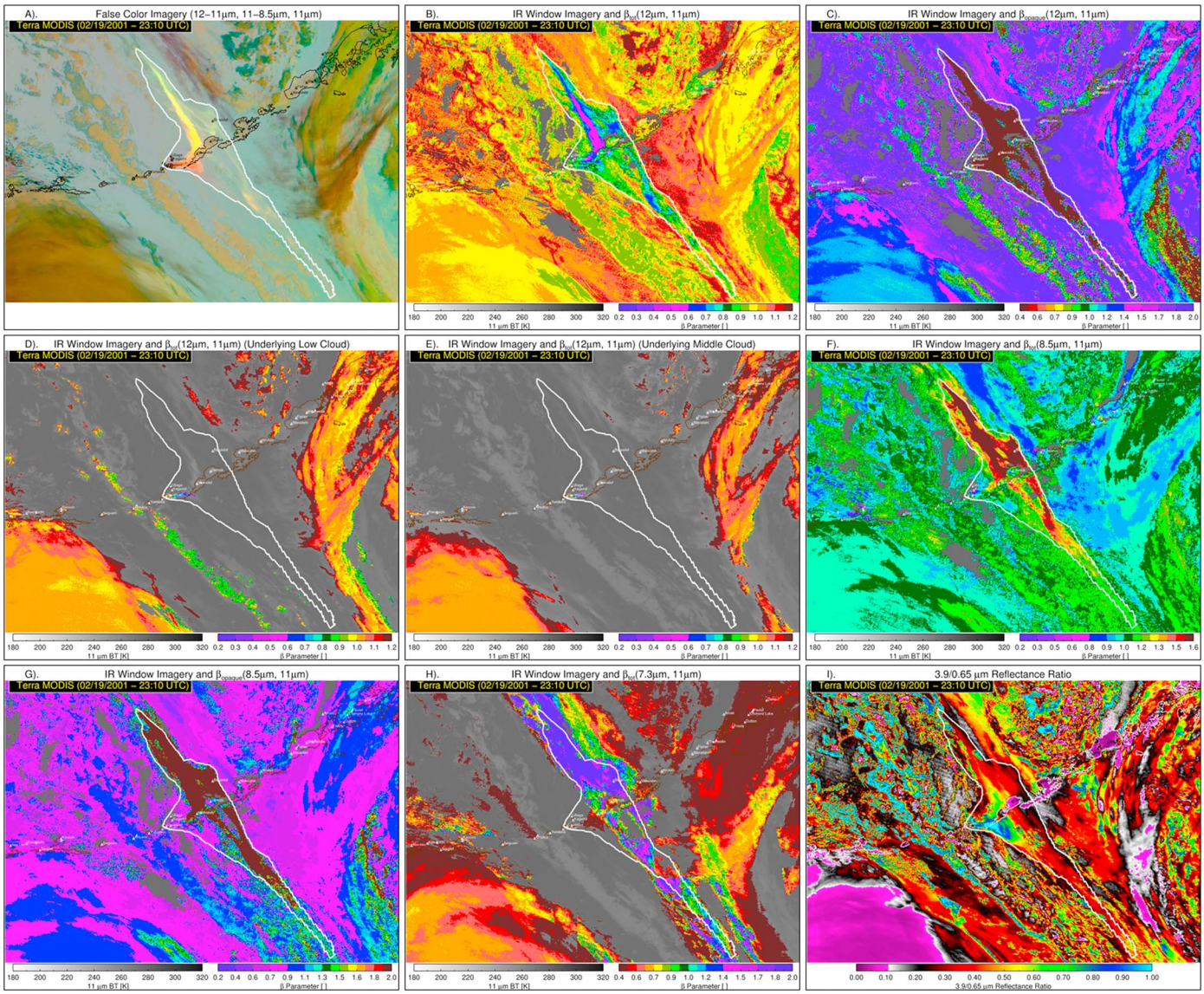

Figure 4. Images of the multispectral classifiers, used during typical sunlit conditions, by the Bayes approach that estimates the probability that a given satellite pixel contains volcanic ash and/or dust are shown. The multispectral parameters were computed for a *Terra* MODIS image from 19 February 2001 at 23:10 UTC. The approximate bounds of an ash cloud produced by an eruption of Mount Cleveland (Alaska) are overlain on each image in white. (a) Multispectral false color image. (b) β_{tot}(12 μm, 11 μm) overlaid on an 11 μm brightness temperature (BT) image. (c) β_{opaque}(12 μm, 11 μm) overlaid on an 11 μm BT image. (d) $\beta_{tot_\sigma 8}$(12 μm, 11 μm) overlaid on an 11 μm BT image. (e) $\beta_{tot_\sigma 7}$(12 μm, 11 μm) overlaid on an 11 μm BT image. (f) β_{tot}(8.5 μm, 11 μm) overlaid on an 11 μm BT image. (g) β_{opaque}(8.5 μm, 11 μm) overlaid on an 11 μm BT image. (h) β_{tot}(7.3 μm, 11 μm) overlaid on an 11 μm BT image. (i) ρ(3.9 μm, 0.65 μm). Only Figures 4b–4i are used as a classifier. Figure 4a is included to aid in scene interpretation. See text and Table 3 for additional details.

ash/dust probability in situations where H_2SO_4 is present. The ash/dust probability can be overestimated further if significant amounts of SO_2 are also present.

Unfortunately, many satellite sensors do not have 7.3 and 8.5 μm channels, but nearly every sensor allows the various forms of β(12 μm, 11 μm) to be paired with near-infrared (day and night) and visible (daytime only) wavelength-based spectral metrics. In the presence of sunlight (when the solar zenith angle is $<85°$ and the measurements are not influenced by sun glint over water), the ratio of the 3.9 μm reflectance and the 0.65 μm reflectance [ρ(3.9 μm, 0.65 μm) = r[3.9 μm]/r[0.65 μm]] can be combined with "split-window" (11 and 12 μm) measurements to distinguish ash and dust clouds from other cloud types [*Pavolonis et al.*, 2006]. Unlike meteorological clouds, the ρ(3.9 μm, 0.65 μm) of volcanic ash and dust clouds tends to increase with decreasing β(12 μm, 11 μm) for a given visible cloud optical depth and set of background conditions. The

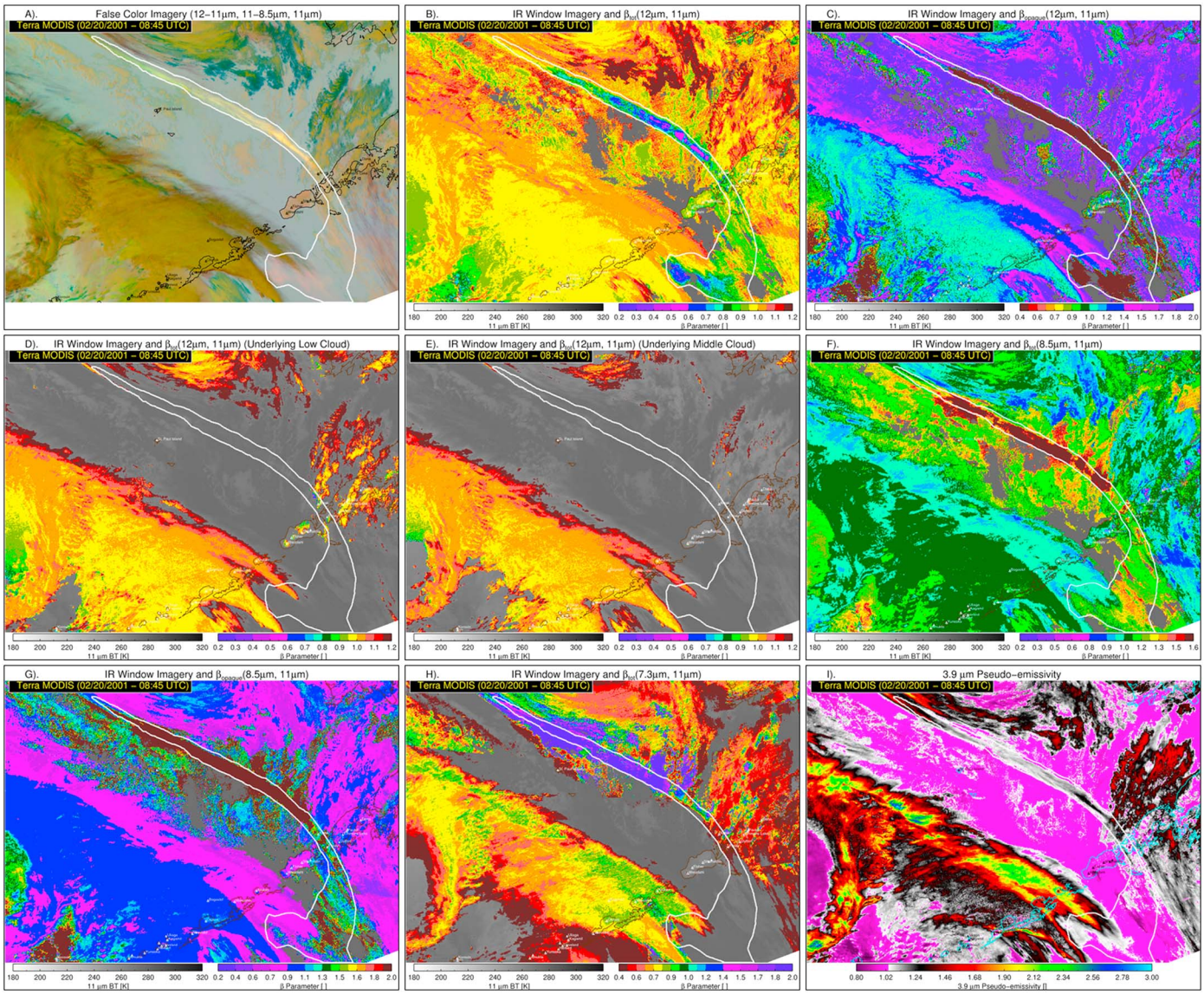

Figure 5. Images of the multispectral classifiers, used at night, by the Bayes approach that estimates the probability that a given satellite pixel contains volcanic ash and/or dust are shown. The multispectral parameters were computed for a *Terra* MODIS image from 20 February 2001 at 08:45 UTC. The approximate bounds of an ash cloud produced by an eruption of Mount Cleveland (Alaska) are overlain on each image in white. (a) Multispectral false color image. (b) β_{tot}(12 μm, 11 μm) overlaid on an 11 μm brightness temperature (BT) image. (c) β_{opaque}(12 μm, 11 μm) overlaid on an 11 μm BT image. (d) $\beta_{tot_\sigma 8}$(12 μm, 11 μm) overlaid on an 11 μm BT image. (e) $\beta_{tot_\sigma 7}$(12 μm, 11 μm) overlaid on an 11 μm BT image. (f) β_{tot}(8.5 μm, 11 μm) overlaid on an 11 μm BT image. (g) β_{opaque}(8.5 μm, 11 μm) overlaid on an 11 μm BT image. (h) β_{tot}(7.3 μm, 11 μm) overlaid on an 11 μm BT image. (i) ε_p(3.9 μm). Only Figures 5b–5i are used as a classifier. Figure 5a is included to aid in scene interpretation. See text and Table 3 for additional details.

ρ(3.9 μm, 0.65 μm) of volcanic ash and dust tends to be >0.5 when the visible cloud optical depth exceeds ~0.10 [*Pavolonis et al.*, 2006]. Meteorological clouds generally have a ρ(3.9 μm, 0.65 μm) < 0.5. The method for computing ρ(3.9 μm, 0.65 μm) along with a more complete description of its utility for ash and dust detection is given by *Pavolonis et al.* [2006]. Figure 4i shows that ρ(3.9 μm, 0.65 μm) within sections of the core of the ash cloud exceeds 0.50, while the ρ(3.9 μm, 0.65 μm) of optically thick meteorological clouds (liquid or ice) is much smaller. However, the edge of meteorological clouds will also have large values of ρ(3.9 μm, 0.65 μm), but this effect is mitigated by pairing ρ(3.9 μm, 0.65 μm) with β(12 μm, 11 μm) in its various forms.

At solar zenith angles greater than 90° and in the absence of stray light influences (significant sunlight impinging on the sensor when the solar zenith angle exceeds 90°), the 3.9 μm pseudoemissivity [ε_p(3.9 μm)] is used in conjunction with β(12 μm, 11 μm) to help identify ash and dust clouds. The ε_p(3.9 μm)

parameter is simply defined as the ratio of the measured 3.9 μm radiance to the estimated 3.9 μm blackbody radiance [ε_p(3.9 μm) = R[3.9 μm]/R_{bb}[3.9 μm]]. As in *Heidinger et al*. [2012], the 3.9 μm blackbody radiance (R_{bb}[3.9 μm]) is estimated by applying the Planck function to the 3.9 μm channel for a given sensor using the measured 11 μm brightness temperature as the blackbody temperature. The ε_p(3.9 μm) parameter is very useful in discriminating between semitransparent clouds and low opaque clouds [*Heidinger et al*., 2012]. Typical behavior of the β(12 μm, 11 μm) and ε_p(3.9 μm) pairing is as follows.

Volcanic ash and dust clouds: β(12 μm, 11 μm) < 1 and ε_p(3.9 μm) > 1
Semitransparent liquid water: β(12 μm, 11 μm) > 1 and ε_p(3.9 μm) > 1
Most ice clouds: β(12 μm, 11 μm) > 1 and ε_p(3.9 μm) > 1
Optically thick liquid water clouds: β(12 μm, 11 μm) < 1 and ε_p(3.9 μm) < 1

Figure 5i shows that ε_p(3.9 μm) of volcanic ash tends to be greater than the ε_p(3.9 μm) of clear sky or opaque low-level and midlevel clouds. While in this particular case, the ε_p(3.9 μm) of semitransparent ice clouds is large compared to volcanic ash, there are instances where the ε_p(3.9 μm) volcanic ash (or dust) and semitransparent ice clouds can be comparable. On sensors that lack the 7.3 and 8.5 μm channels, β(12 μm, 11 μm) is not coupled with any other *multispectral* parameters in the day/night terminator region (solar zenith angle between 85 and 90°).

Each multispectral radiative parameter pairing is best used in conjunction with an indicator of how much the observed radiance deviates from the estimated clear-sky radiance. As in *Heidinger et al*. [2012], the 11 μm emissivity value a cloud would have if it were located at the top of the thermodynamically defined troposphere [ε_{tot}(11 μm)] is used to quantify the confidence that a given multispectral signature is associated with a cloud and not a clear-sky feature (e.g., the surface). As will be described in a later section, additional spatial analysis techniques are utilized to mitigate the impacts of errors in the clear-sky radiance calculations. Clear-sky radiance errors can be large [*Heidinger and Pavolonis*, 2009], particularly over land where the uncertainty in surface temperature and emissivity is significant.

4.2. Naïve Bayesian Approach

While the various multispectral metrics described in the previous section are useful for detecting volcanic ash and dust, the relationship between each spectral metric is quite complicated. In an effort to sufficiently capture the complicated multispectral relationships over a wide range of conditions and reduce the many pieces of spectral information into a single objective metric, a Bayesian approach is utilized. Bayesian approaches have been successfully applied to several satellite-based classification problems [*Uddstrom et al*., 1999; *Merchant et al*., 2005; *Heidinger et al*., 2012; *Kossin and Sitkowski*, 2009; *Cintineo et al*., 2014; *Mackie and Watson*, 2014]. As discussed by *Kossin and Sitkowski* [2009] and *Heidinger et al*. [2012], the classical Bayesian approach is not practical when more than just a few features are used, as the size of the class conditional probability density functions can easily grow to an unmanageable size and become very difficult to sufficiently populate. Thus, in lieu of the classical implementation of the Bayesian approach [*Uddstrom et al*., 1999; *Merchant et al*., 2005], a Naïve Bayesian approach [*Heidinger et al*., 2012; *Kossin and Sitkowski*, 2009; *Cintineo et al*., 2014] is used. The naïve Bayesian model is formulated by assuming that features (***F***) are independent within each class. The naïve Bayes classifier has been shown to perform quite well even when the features are clearly not independent [*Domingos and Pazzani*, 1997; *Hand and Yu*, 2001; *Kossin and Sitkowski*, 2009; *Heidinger et al*., 2012; *Cintineo et al*., 2014]. Using the naïve Bayes formulation, the probability of ash or dust given an observed set of independent features ($P(C_{yes}|\boldsymbol{F})$ is calculated using equation (5) (the term, $P(C_{yes}|\boldsymbol{F})$, is also commonly referred to as the posterior probability).

$$P\left(C_{yes}|\boldsymbol{F}\right) = \frac{P\left(C_{yes}\right)\prod_{i=1}^{N} P\left(F_i\,|C_{yes}\right)}{P(\boldsymbol{F})} \tag{5}$$

In equation (5), $P(C_{yes})$ is the prior probability that a given satellite pixel contains volcanic ash or dust without knowledge of ***F***, $P(F_i|C_{yes})$ is the estimated probability of observing a given feature (F_i) when ash or dust are present (a total of N features are used), and $P(\boldsymbol{F})$ is the probability of a given set of features being observed and is computed using equation (6).

$$P(\boldsymbol{F}) = P\left(C_{yes}\right)\prod_{i=1}^{N} P\left(F_i|C_{yes}\right) + P(C_{no})\prod_{i=1}^{N} P(F_i|C_{no}) \tag{6}$$

In equation (6), $P(C_{no})$ is the prior probability that a given satellite pixel does *not* contain volcanic ash or dust [e.g., $P(C_{no}) = 1 - P(C_{yes})$] and $P(F_i|C_{no})$ is the estimated probability of observing a given feature (F_i) when ash or dust is *not* present.

The prior probability of ash/dust [$P(C_{yes})$] is assumed to be 0.1%, which, while arbitrary and crude, roughly captures the fact that the global fractional coverage of ash or dust that *is detectable using passive satellite measurements* is generally small relative to all other observable cloud and surface features. In addition, the ash/dust conditional probability is often many orders of magnitude greater than the nonash/nondust conditional probability, rendering the impact of the prior probabilities minimal. Further, in our application, the posterior probability is largely used to determine cloud object membership (e.g., whether or not a given pixel should be used when constructing cloud objects) [*Pavolonis et al.,* 2015] and the use of constant prior probabilities ensures that it is purely the multispectral signature at a given time that influences cloud object membership for a given probability threshold, not the prior probabilities. Thus, we avoided using prior probabilities that depend on time and geographic location but acknowledge that the climatological probability of ash/dust is likely several orders of magnitude greater near source regions than locations far removed from dust source regions or volcanoes that frequently produce ash clouds (e.g., Sakurajima, Japan).

The class conditional probability density functions (PDFs), the dimensions of which are subsequently described, are empirically constructed for each classifier (F_i) from a large training data set. The "yes" class training data set consists of 344 5 min MODIS granules (see Table S1, supporting information) with ash and/or dust clouds, the horizontal bounds of which were manually analyzed by a human expert using the same type of false color images described earlier and region of interest (ROI) software applications. Only situations where ash/dust clearly was the highest cloud layer were classified as ash/dust during the manual analysis process. In addition, cloud edges were drawn with an emphasis on avoiding false alarms (cross-contamination) at the expense of excluding a small number of ash/dust pixels. The 344 ash/dust cases (305 ash scenes and 39 dust scenes) were selected so that a large number of background (surface and atmosphere) and ash/dust cloud states were sampled. For instance, low-, middle-, and high-latitude eruptions of varying intensity (and varying SO_2 emissions) were selected and an effort was made to ensure that a diverse set of underlying surfaces and clouds was sampled. MODIS scenes composed of resuspended ash [e.g., *Hadley et al.*, 2004] were also included. North American, African, Asian, and Australian dust clouds were sampled.

The training database for the "yes" class consists of about 6.5 million volcanic ash pixels and 3.7 million desert dust pixels, after applying several quality control measures and simple filters. The quality control measures and filters are described shortly. Even though the number of dust cloud pixels in the training data set is less than the number of ash cloud pixels, the method performs well when applied to dust clouds because ash and dust have similar spectral signatures in the broadband to narrowband spectral channels that the SECO method utilizes, and the range of dust cloud property states is likely smaller than the range of ash cloud property states because ash clouds are the result of complex, and highly variable, volcanological processes interacting with a wide range of complex and highly variable atmospheric processes.

A total of about 2.5 billion nonvolcanic ash/dust pixels (after quality control and filtering), drawn from 2401 different 5 min MODIS granules, were used to construct the training database for the "no" class. To avoid cross-contamination, the nonash/nondust training pixels were taken from MODIS granules that were independent of those used to construct the ash/dust component of the training. In fact, each of the 2401 5 min MODIS granules used to build the "no" class training was deemed to be totally free of detectable ash or dust clouds through manual inspection of false color imagery. Global or near-global coverage was achieved for one day per month from November 2009 to October 2010 using both the *Terra* (midmorning sun synchronous orbit) and *Aqua* (midafternoon sun synchronous orbit) satellites.

Despite the large size of the training data set, some portions of the various PDFs were not sampled. The unsampled regions were consistent with physical expectations. Conditional probabilities cannot be equal to zero, so the observational count in every PDF bin was increased by a constant noninteger factor such that unsampled PDF bins produce ash/dust and nonash/nondust conditional probabilities that are identical (the noninteger factor has no impact on the ratio between the "yes" and "no" class conditional

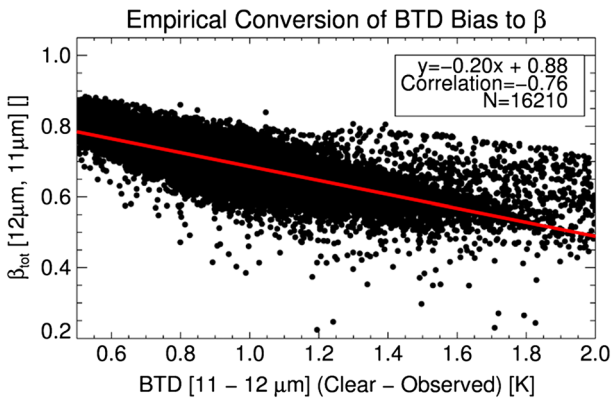

Figure 6. The empirical relationship used to estimate the top of troposphere referenced 12/11 μm effective absorption optical depth ratio [β_{tot}(12 μm, 11 μm)] from the clear minus observed 11–12 μm brightness temperature difference (BTD) is shown.

probabilities in the bins that already contained observations). This simple step is needed to prevent arithmetic overflow and gracefully default to the prior probability in the rare event that the unsampled portions of the PDF are observed when applied to satellite data not included in the training data set. In the future, additional training cases can also be added should there be a need.

The nonvolcanic ash/dust component of the training data will consist of clear and cloudy pixels, as no cloud mask was applied. The ash/dust training data may also contain a very small fraction of clear pixels due to smoothing of cloud edges as an unavoidable consequence of the manual analysis process. A cloud mask algorithm was not used to filter out clear pixels because all available algorithms classify volcanic ash and dust pixels as "clear" to varying degrees. All pixels, however, were required to have a ε_{tot}(11 μm) ≥ 0.02, which ensures that pixels that have an observed 11 μm radiance that deviates very little from the estimated 11 μm clear-sky radiance do not negatively influence the classifier training or the implementation of the SECO algorithm. This step eliminates many of the clear pixels without having to apply a separate cloud mask algorithm.

There are instances, however, where the ε_{tot}(11 μm) of ash or dust clouds, which are identifiable in multispectral imagery, is less than 0.02 or even negative (the observed radiance is greater than the calculated clear-sky radiance) due to errors in the clear-sky radiance calculation or temperature inversion effects, especially over land surfaces. Errors in the numerical weather prediction supplied surface temperature can be quite large [*Heidinger and Pavolonis*, 2009] over land surfaces. When the surface temperature is underestimated, the clear-sky radiance for a given surface-viewing channel (e.g., 11 and 12 μm) will also be underestimated, sometimes causing the observed radiance to be greater than the clear-sky radiance, even under cloudy conditions. Errors in the surface temperature impact the calculation of the clear-sky radiance at 11 and 12 μm similarly enough that the bias (calculated − observed) in the calculated clear-sky 11–12 μm BTD under observed clear-sky conditions is much less than the clear-sky brightness temperature bias in either channel alone. As such, the calculated clear sky minus the observed 11–12 μm BTD (hereafter referred to as BTD_Bias) can be empirically related to β_{tot}(12 μm, 11 μm) for ash/dust clouds that have an observed 11 μm radiance that does not strongly deviate from the clear-sky radiance or in situations where the clear-sky radiance is less than the observed radiance due to errors in the clear-sky calculation and/or temperature inversion effects. The linear regression relationship shown in Figure 6 is used to "restore" potential volcanic ash and dust pixels that have a ε_{tot}(11 μm) < 0.02, a BTD_Bias > 0.5 K, and an observed 11–12 μm BTD < 0 K. *Francis et al.* [2012] and *Pavolonis et al.* [2013] also utilized the BTD_Bias to aid in ash detection. A subset of the over-land volcanic ash/dust training data with 0.02 < ε_{tot}(11 μm) < 0.08 was used to construct the relationship shown in Figure 6. The ε_{tot}(11 μm) < 0.02 screening rule and the empirical conversion of BTD_Bias to β_{tot}(12 μm, 11 μm) are also utilized during the practical implementation of the SECO algorithm.

Four simple multispectral filters are also applied to eliminate pixels from the "yes" and "no" training data that have a "split-window" signature that is strongly inconsistent with ash/dust and is likely the result of the human expert's inability to exactly define the edge of ash and dust clouds in multispectral imagery during the manual analysis process. The following filters are also applied during the practical implementation of the SECO algorithm.

1. All pixels with a β_{tot}(12 μm, 11 μm) value of >1.05, which is slightly greater than the upper theoretical limit for volcanic ash and dust [*Pavolonis*, 2010; *Pavolonis et al.*, 2013], are excluded from the "yes" and "no" training data.

2. All pixels must also have a 11–12 μm BTD that is less than the BTD_MAX (see equation (7)), which corresponds to the 99th percentile value from the ash/dust training data set as a function of ε_{tot}(11)m). This filter function is designed to mitigate the impacts of possible errors associated with manually defining the edge of ash and dust clouds when $\varepsilon_{tot}(11\ \mu m) \geq 0.5$.

$$BTD_{MAX} = \begin{cases} -1.19\varepsilon_{tot}(11\ \mu m) + 1.14, & 0.5 \leq \varepsilon_{tot}(11\ \mu m) \leq 1.0 \\ 1000.0, & \varepsilon_{tot}(11\ \mu m) < 0.5 \end{cases} \tag{7}$$

3. All pixels must also have a BTD_Bias that is greater than BTD_BIAS_MIN (see equation (8)), which corresponds to the 1st percentile value from the ash/dust training data set as a function of ε_{tot}(11 μm). This filter function is designed to mitigate the impacts of possible errors associated with manually defining the edge of ash and dust clouds when $\varepsilon_{tot}(11\ \mu m) < 0.5$.

$$BTD_{BIAS}MIN = \begin{cases} -0.70\varepsilon_{tot}(11\ \mu m) + 0.03, & 0.0 \leq \varepsilon_{tot}(11\ \mu m) < 0.5 \\ -1000.0, & \varepsilon_{tot}(11\ \mu m) \geq 0.5 \end{cases} \tag{8}$$

4. All pixels with an observed 11–12 μm BTD > 0 K must also have a β_{opaque}(12 μm, 11 μm) value of <1.36, which is the 99th percentile value from the ash/dust training data set.

The 11–12 μm BTD ("split-window") attributes of the quality-controlled and filtered training data were analyzed to help quantify the limitations of traditional "split-window" ash/dust detection approaches and to help illustrate that the training data are representative of a wide range of conditions. The relative and absolute distributions of the 11–12 μm BTD for the ash/dust ("yes") and nonash/nondust ("no") classes are shown in Figure 7. The distributions clearly indicate that there is significant overlap between the two classes such that even 11–12 μm BTD values of −1 K are not totally unique to ash and dust clouds. In addition, many volcanic ash/dust pixels do not exhibit a negative "split-window" signature likely due to influences from background water vapor and/or cloud microphysical effects. While traditional threshold-based "split-window" ash/dust detection algorithms are very simple to implement and may work well for a single case with a limited geographic extent, Figure 7c shows that the when applied to a global, multiseason data set, the detection skill (quantified using the critical success index) of those algorithms is extremely limited. The critical success index (CSI) is defined as the number of hits divided by the sum of hits, false alarms, and misses. The CSI does not take correct negatives into account, so it is an effective metric when the event of interest is observed far less often than the nonevents and the tolerance for false alarms is low (volcanic ash false alarms are particularly undesirable). The maximum CSI of a threshold-based "split-window" algorithm applied to our extensive training data set is about 0.20 when a threshold of −1.25 K is used. The probability of detection (POD) for a threshold of −1.25 K is only about 0.30 with a false alarm rate (FAR) of 0.002.

The features or classifiers (F_i) used in our Bayes implementation are listed in Table 3 as a function of satellite sensor. Even though the naïve Bayes formulation allows us to assume that each feature or classifier is independent, we utilize multivariate classifiers. The two- and three-dimensional classifiers are very effective at capturing the most robust spectral indicators of ash and dust (see earlier discussion) without requiring large PDFs. Our methodology still takes advantage of the independence assumption, as we utilize far more than two or three predictors, which would not be practical without the naïve Bayes formulation. The conditional probabilities for each class are estimated from histograms of the training data set. The histogram bins are defined in Table 3.

Classifiers that are directly influenced by reflected sunlight were parsed into three different surface-type categories (open water, snow/ice, and non-snow/ice land surfaces), while classifiers not directly influenced by reflected sunlight were sorted into two different surface-type categories (open water and solid surfaces). Daily global snow/ice maps were constructed by combining the 4 km Interactive Multisensor Snow and Ice Mapping System [*Ramsay*, 1998], which at the time of this writing only provides coverage of the Northern Hemisphere, with the 25 km Special Sensor Microwave Imager-Special Sensor Microwave Imager/Sounder global ice concentration and snow extent data set [*Nolin et al.*, 1998] to fill in the Southern Hemisphere. The surface types were chosen to broadly account for surface albedo effects on visible and near-infrared measurements during the day and differences in clear-sky infrared radiative transfer error characteristics (errors are generally larger over land than open water). In addition, the classifiers

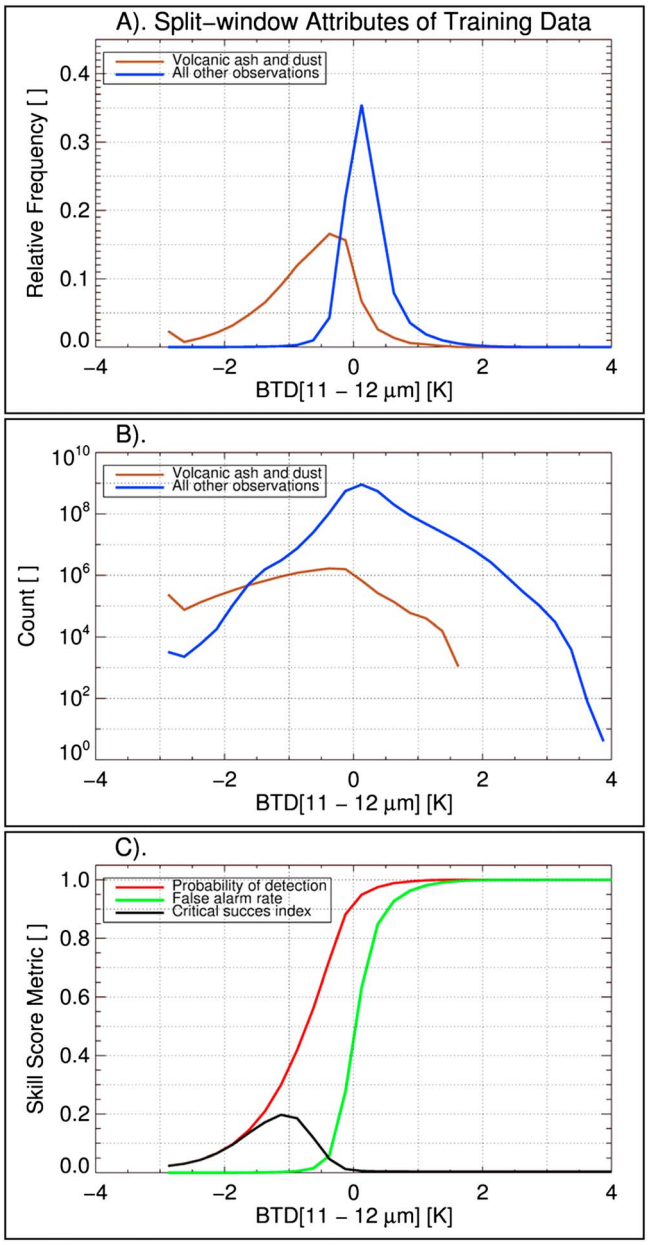

Figure 7. (a) Normalized distribution of the 11–12 μm brightness temperature difference (BTD) of the data used to derive the ash/dust and the nonash/nondust class conditional probabilities. (b) Same as Figure 7a, except the distribution is not normalized and is shown using a log *y* axis. (c) Skill statistics of a simple threshold-based 11–12 μm BTD ash/dust detection approach, applied to the training data set, is plotted as a function of the chosen threshold (classified as ash/dust if 11–12 μm BTD ≤ threshold on the *x* axis). The probability of detection (red), false alarm rate (green), and critical success index (black) are shown.

that depend on ρ(3.9 μm, 0.65 μm) are also parsed into two scattering angle (Θ) categories ($\Theta < 90°$ and $\Theta \geq 90°$) to roughly account for differences in the 0.65 and 3.9 μm scattering phase functions. The scattering angle is defined as

$$\Theta = \cos^{-1}\left(-\cos\theta_{sun}\cos\theta_{sat} + \sin\theta_{sun}\sin\theta_{sat}\cos\varnothing\right) \quad (9)$$

where θ_{sun} is the solar zenith angle, θ_{sat} is the satellite zenith angle, and $\varnothing$ is the relative azimuth angle. Experiments were conducted using more than two Θ categories, but the results changed very little.

The SECO algorithm utilizes five to eight classifiers, depending on the spectral channels provided by a given sensor. Each classifier has ε_{tot}(11 μm) as the outermost dimension since uncertainties in the clear-sky radiative transfer calculations influence the interpretation of the multispectral parameters [*Pavolonis et al.*, 2006; *Pavolonis*, 2010; *Pavolonis et al.*, 2013]. When the solar zenith angle is less than 85° and sun glint is not present, four different varieties of β(12 μm, 11 μm) are paired with ρ(3.9 μm, 0.65 μm) (see Table 3). Sun glint is deemed to be present if the pixel is located over open water and the glint angle (Θ_{glint}) is greater than 40°. The glint angle is defined in equation (10).

$$\Theta_{glint} = \cos^{-1}\left(\cos\theta_{sun}\cos\theta_{sat} + \sin\theta_{sun}\sin\theta_{sat}\cos\varnothing\right) \quad (10)$$

It is important to note that the relationship between any two forms of $\beta(\lambda_1, \lambda_2)$, produced using the same λ_1 and λ_2, is highly nonlinear [*Heidinger et al.*, 2010], so each form of β(12 μm, 11 μm) coupled with ρ(3.9 μm, 0.65 μm) will produce a different conditional probability. From a physical standpoint, each form of β(12 μm, 11 μm) describes a different part of the solution space that defines which cloud property states are possible given the measurements (and associated noise) and the clear-sky radiative transfer modeling (and associated errors). For additional discussion of the cloud property solution space in the infrared, consult *Heidinger et al.* [2010] and *Pavolonis* [2010]. When the solar zenith angle (θ_{sun}) is greater than 90°, the same four varieties of β(12 μm, 11 μm) are paired with ε_p(3.9 μm). In the day/night terminator region ($85° \leq \theta_{sun} \leq 90°$) and in sun glint, a ε_{tot}(11 μm) × β(12 μm, 11 μm) multivariate classifier is used. In addition, the ε_{tot}(11 μm) × β_{tot}(12 μm, 11 μm) × β_{tot}(8.5 μm, 11 μm), ε_{tot}(11 μm) × β_{opaque}(12 μm, 11 μm) × β_{opaque}(8.5 μm, 11 μm), and ε_{tot}

Table 3. The Leftmost Portion of the Table Lists the Individual Radiative Parameters Utilized to Construct SECO Algorithm Classifiers, Along With the Corresponding Histogram Binning Scheme Used to Estimate the Classifier PDFs[a]

Parameter [Parameter ID]	Number of Histogram Bins	Starting Boundaries of Histogram Bins
ε_{tot}(11 μm) [1]	6	0.01, 0.03, 0.10, 0.20, 0.50, 0.90
β_{tot}(12 μm, 11 μm) [2]	42	−0.10 to 1.95 in increments of 0.05
β_{opaque}(12 μm, 11 μm) [3]	42	−0.10 to 1.95 in increments of 0.05
$\beta_{tot_\sigma 8}$(12 μm, 11 μm) [4]	42	−0.10 to 1.95 in increments of 0.05
$\beta_{tot_\sigma 7}$(12 μm, 11 μm) [5]	42	−0.10 to 1.95 in increments of 0.05
β_{tot}(8.5 μm, 11 μm) [6]	21	−0.10 to 1.90 in increments of 0.10
β_{opaque}(8.5 μm, 11 μm) [7]	21	−0.10 to 1.90 in increments of 0.10
β_{tot}(7.3 μm, 11 μm) [8]	21	−0.10 to 1.90 in increments of 0.10
ρ(3.9 μm, 0.65 μm) [9]	13	0.00 to 1.20 in increments of 0.10
ε_p(3.9 μm) [10]	25	0.80 to 2.00 in increments of 0.05
BTD(11-12 μm) [11]	33	−3.0 to 5.0 in increments of 0.25 K
Multivariate Classifier Arrays	**Relevant Sensors**	**Conditions**
[1] × [2] × [9] [1] × [3] × [9] [1] × [4] × [9] [1] × [5] × [9] [1] × [11] × [9]	AVHRR[b] COMS-MI GOES-Imager[c] GOES-R ABI Himawari-8/9 AHI MODIS MTSAT Imager MSG SEVIRI MTG FCI VIIRS	Only applied outside of sun glint when the solar zenith angle is less than 85°.
[1] × [2] × [10] [1] × [3] × [10] [1] × [4] × [10] [1] × [5] × [10] [1] × [11] × [10]	AVHRR[b] COMS-MI GOES-Imager[c] GOES-R ABI Himawari-8/9 AHI MODIS MTSAT Imager MSG SEVIRI MTG FCI VIIRS	Only applied when the solar zenith angle is greater than 90° and stray light is not detected.
[1] × [2] × [6] [1] × [3] × [7]	GOES-R ABI Himawari-8/9 AHI MODIS MSG SEVIRI MTG FCI VIIRS	Applied at all times.
[1] × [2] × [8]	GOES-R ABI Himawari-8/9 AHI MODIS MSG SEVIRI MTG FCI	Applied at all times.
[1] × [2] [1] × [3] [1] × [4] [1] × [5] [1] × [11]	AVHRR[b] COMS-MI GOES-Imager[c] GOES-R ABI Himawari-8/9 AHI MODIS MTSAT Imager MSG SEVIRI MTG FCI VIIRS	Only applied when both ρ(3.9 μm, 0.65 μm) and ε_p(3.9 μm) are invalid.

[a]The multivariate classifier arrays (using the radiative parameter IDs shown in the left part of the table) are listed in the right part of the table as a function of satellite sensor and the conditions required for utilization. Sun glint is assumed to be present over water surfaces if the glint angle is less than 40°. Stray light is assumed to be present if the solar zenith angle exceeds 90° and the measured 0.65 μm count is greater than a sensor-dependent threshold. Please see Table 2 for a list of sensor acronyms.

[b]The analogue to the 3.9 μm band on AVHRR (the 3.75 μm band) is currently not available on the MetOp-A and MetOp-B spacecraft during daytime operations.

[c]The 12 μm channel is only available on the GOES 8–11 spacecraft.

(11 μm) × β_{tot}(12 μm, 11 μm) × β_{tot}(7.3 μm, 11 μm) classifiers are used at all times of the day if the sensor spectral capabilities allow. While β(12 μm, 11 μm) has been demonstrated to be a more robust metric for inferring cloud composition than the 11–12 μm BTD [*Pavolonis*, 2010], multivariate 11–12 μm BTD-based classifiers are also used as there are occasions when the β(12 μm, 11 μm)-based metrics are less skillful either due to errors in clear-sky radiative transfer modeling or due to "saturation" issues at large cloud optical depths. The 11–12 μm BTD-based classifiers are only used when the 11–12 μm BTD is less than zero and the BTD data are parsed into five different 11 μm clear-sky brightness temperature bins (<255 K, 255–260 K, 260–265 K, 265–270 K, and >270 K) to account for the increased frequency of occurrence of negative "split-window" values in environments with cold backgrounds [*Pavolonis et al.*, 2006].

By taking the ratio of the ash/dust conditional probability to the nonash/nondust conditional probability for each bin in the conditional probability lookup table, regions of the multivariate classifier space that favor volcanic ash/dust can be easily visualized. Figure 8 shows the conditional probability ratio of all of the multivariate classifiers used over open water surfaces. In addition, Figures 8a–8d are valid for $\Theta \geq 90°$. Only the 0.10–0.20 ε_{tot}(11 μm) bin is shown for the three-dimensional classifiers (Figures 8a–8). The cyan to red portion of the color scheme is indicative of histogram bins where the ash/dust conditional probability is larger than the nonash/nondust conditional probability. Figure 8 indicates that the relationship between a given pair of multispectral variables is generally complicated and not conducive to using simple threshold functions to identify ash and dust in a deterministic manner. While β_{tot}(12 μm, 11 μm) must have a valid value in order to estimate the ash/dust probability for a given satellite pixel, all other variants of $\beta(\lambda_1, \lambda_2)$ are allowed to be invalid ($\varepsilon(\lambda_1)$ and/or $\varepsilon(\lambda_2) < 0.0$), as an invalid $\beta(\lambda_1, \lambda_2)$ is still informative. For instance, an invalid $\beta_{tot_\sigma 8}$(12 μm, 11 μm) is more likely to be associated with a single-layer cloud than a valid value of $\beta_{tot_\sigma 8}$ (12 μm, 11 μm). All invalid $\beta(\lambda_1, \lambda_2)$ values are placed in the very first histogram bin for that particular $\beta(\lambda_1, \lambda_2)$. It is also worth noting that due to the maximum emissivity being capped at 0.99990 as a means of preventing arithmetic overflow when computing cloud optical depth (see equation (3)), the minimum valid value of $\beta_{opaque}(\lambda_1, \lambda_2)$ is approximately 0.425 (e.g., $\varepsilon(\lambda_1) = 0.98$ per the definition of the opaque cloud assumption and $\varepsilon(\lambda_2) = 0.99990$ per the maximum allowed value).

As might be expected, the three-dimensional classifiers (Figures 8a–8k) can provide greater spectral separation between ash/dust and all other features in the training data set compared to the two-dimensional (bispectral) classifiers (Figures 8l–8o). Fortunately, the two-dimensional classifiers are only utilized under a very limited set of conditions. Figure 8 also reveals that the classifiers that utilize the top of troposphere variant of $\beta(\lambda_1, \lambda_2)$ provide the best opportunity to produce an ash/dust conditional probability that is 1000–10,000 times *larger* than the nonash/nondust conditional probability. In contrast, the classifiers that utilize an "opaque cloud" version of $\beta(\lambda_1, \lambda_2)$ generally provide the best opportunity to produce an ash/dust conditional probability that is 1000–10,000 times *smaller* than the nonash/nondust conditional probability. The β_{tot}(12 μm, 11 μm) × β_{tot} (8.5 μm, 11 μm) classifier (Figure 8i) has two distinct regions where the ash/dust conditional probability is at least 100 times greater than the nonash/nondust conditional probability. The dual-maxima structure is primarily the result of small amounts of SO_2 combining with volcanic ash to create a spectral signature that is very similar to low-level liquid water clouds. The dual-maxima pattern is most pronounced when ε_{tot} (11 μm) < 0.10 (not shown), rendering the β(8.5 μm, 11 μm)-based classifiers (Figures 8i and 8j) less useful in the transition region between little to no SO_2 influence and strong SO_2 influence. Thus, the β(8.5 μm, 11 μm)-based classifiers are not used unless ε_{tot}(11 μm) > 0.10 or β_{tot}(8.5 μm, 11 μm) ≤ 1.05 or β_{tot}(8.5 μm, 11 μm) ≥ 2.0.

Over land surfaces, the classifiers that do not rely on the presence of sunlight exhibit ash/dust conditional probabilities that are rarely more than 1000 times larger than the corresponding nonash/nondust conditional probability (not shown). The differences between the land and water conditional probabilities can be largely attributed to the greater uncertainty in the clear-sky radiance calculations over land. Over snow and ice surfaces, ρ(3.9 μm, 0.65 μm) is very small under clear-sky conditions because snow and ice have a very large albedo at 0.65 μm and a very small albedo at 3.9 μm, further reducing the ratio between the ash/dust conditional probability and the nonash/nondust conditional probability. The difference between surface types (land versus water versus snow) becomes much smaller with increasing ε_{tot}(11 μm). Finally, the conditional probability ratios for the 11–12 μm BTD-based classifiers are highly negative "split-window" values. Far less separation between ash/dust and all other features is found when the 11–12 μm BTD is about −0.5 K or larger. Additional details on the conditional probability ratios can be found in *Pavolonis* [2014].

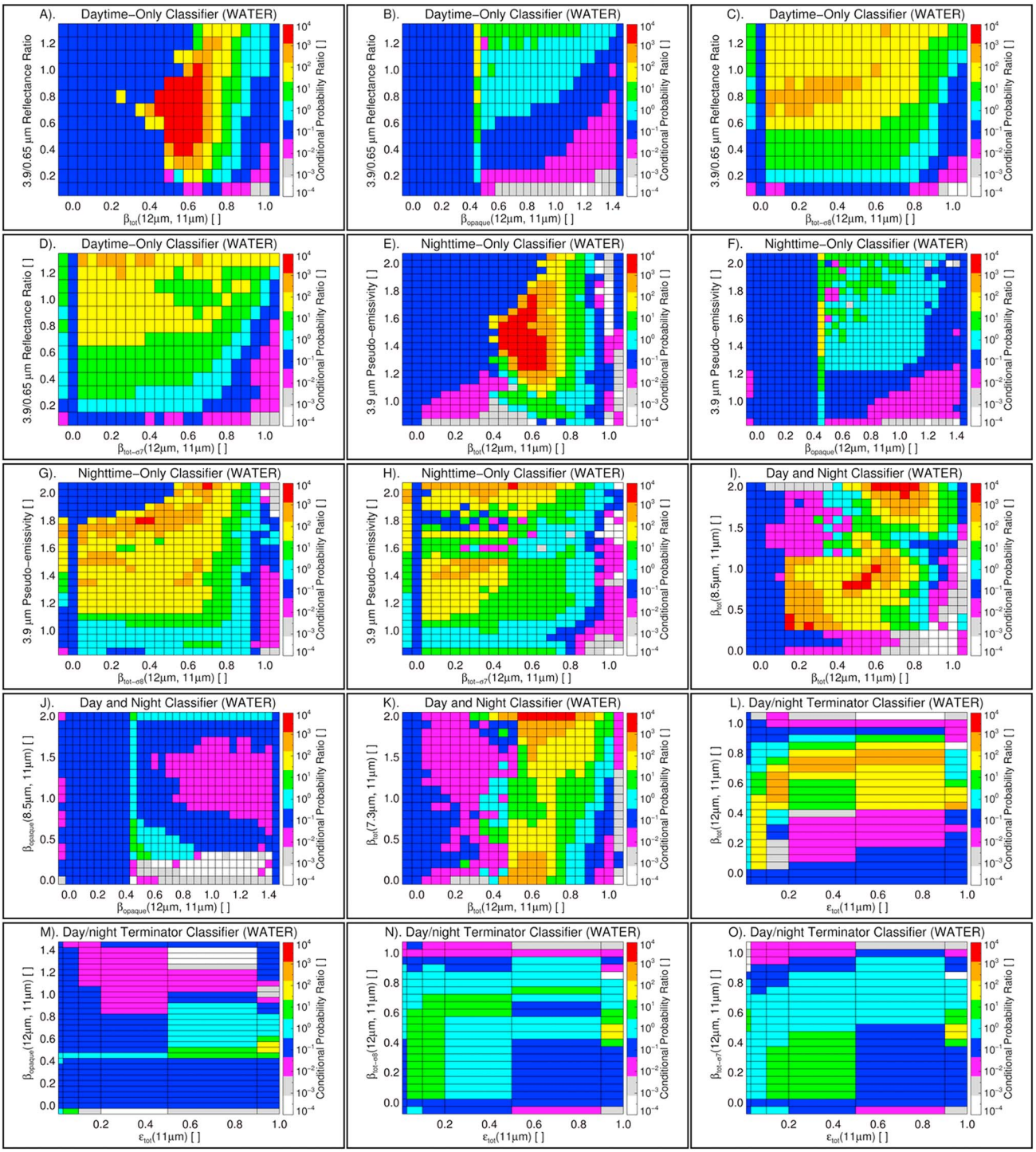

Figure 8. The ratio of the ash/dust class conditional probability to the class conditional probability of all other features is shown as a function of various multivariate spectral classifiers for an open water surface. The cyan through red portion of the color scheme indicates that the class conditional probability of ash/dust is greater than the class conditional probability of all nonash/nondust features for that histogram bin. (a) β_{tot}(12 μm, 11 μm) versus ρ(3.9 μm, 0.65 μm) (daytime classifier), (b) β_{opaque}(12 μm, 11 μm) versus ρ(3.9 μm, 0.65 μm) (daytime classifier), (c) $\beta_{tot_\sigma 8}$(12 μm, 11 μm) versus ρ(3.9 μm, 0.65 μm) (daytime classifier), (d) $\beta_{tot_\sigma 7}$(12 μm, 11 μm) versus ρ(3.9 μm, 0.65 μm) (daytime classifier), (e) β_{tot}(12 μm, 11 μm) versus ε_p(3.9 μm) (nighttime classifier), (f) β_{opaque}(12 μm, 11 μm) versus ε_p(3.9 μm) (nighttime classifier), (g) $\beta_{tot_\sigma 8}$(12 μm, 11 μm) versus ε_p(3.9 μm) (nighttime classifier), (h) $\beta_{tot_\sigma 7}$(12 μm, 11 μm) versus ε_p(3.9 μm) (nighttime classifier), (i) β_{tot}(12 μm, 11 μm) versus β_{tot}(8.5 μm, 11 μm) (day and night classifier), (j) β_{opaque}(12 μm, 11 μm) versus β_{opaque}(8.5 μm, 11 μm) (day and night classifier), (k) β_{tot}(12 μm, 11 μm) versus β_{tot}(7.3 μm, 11 μm) (day and night classifier), (l) ε_{tot}(11 μm) versus β_{tot}(12 μm, 11 μm) (twilight classifier only), (m) ε_{tot}(11 μm) versus β_{opaque}(12 μm, 11 μm) (twilight classifier only), (n) ε_{tot}(11 μm) versus $\beta_{tot_\sigma 8}$(12 μm, 11 μm) (twilight classifier only), (o) ε_{tot}(11 μm) versus $\beta_{tot_\sigma 7}$(12 μm, 11 μm) (twilight classifier only). Figures 8a–8k are valid for $0.10 < \varepsilon_{tot}(11\ \mu m) < 0.20$.

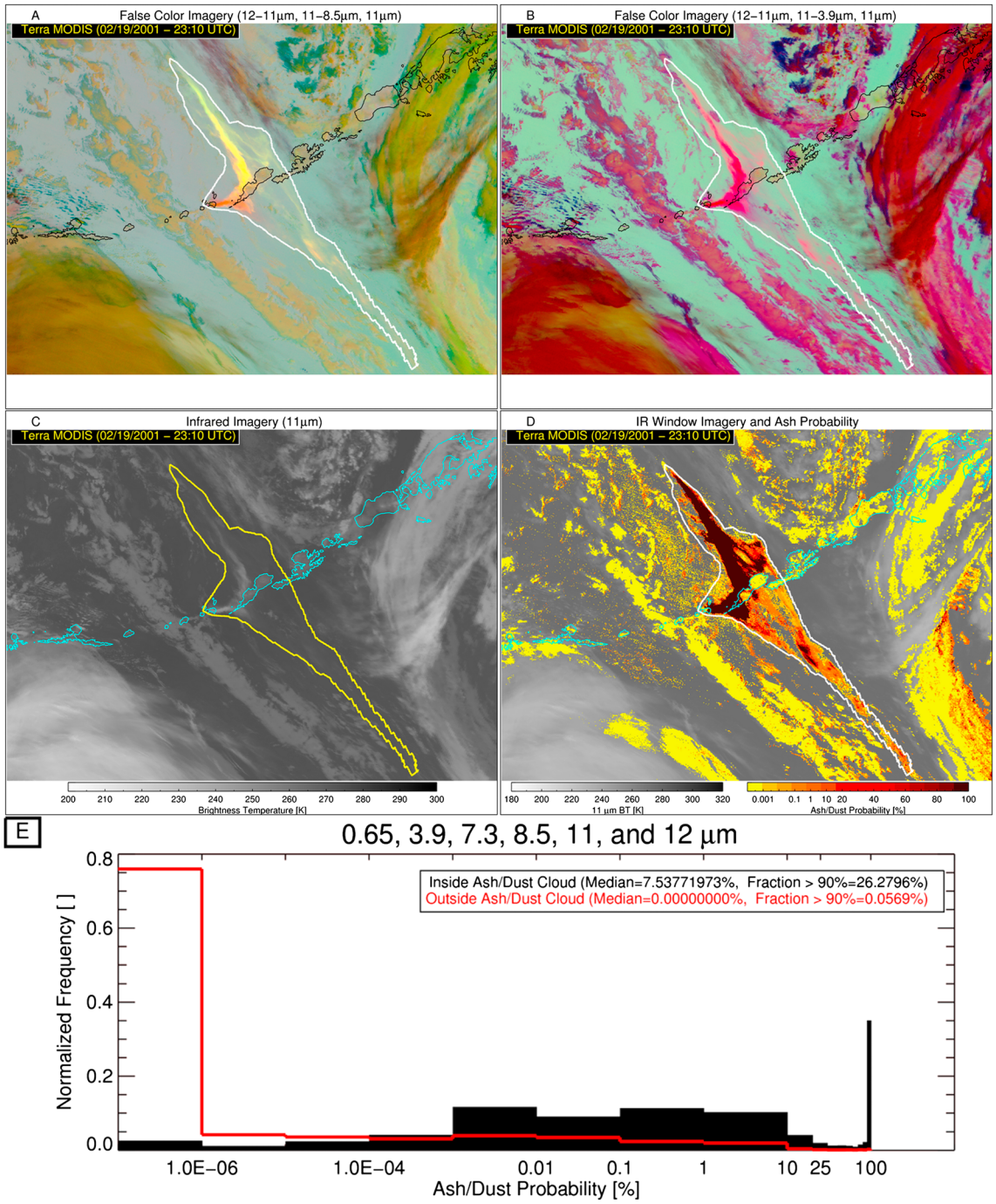

Figure 9. The results of the Bayesian method are shown for a *Terra* MODIS image from 19 February 2001 at 23:10 UTC. (a) 12–11 μm, 11–8.5 μm, and 11 μm false color image. (b) 12–11 μm, 11–3.9 μm, and 11 μm false color image. (c) 11 μm image. (d) Ash/dust probability image for 0.65, 3.9, 7.3, 8.5, 11, and 12 μm channel combination. (e) Histogram of ash/dust probability inside (black) and outside (red) of manually analyzed ash/dust cloud. The outer bounds of the manually defined ash/dust cloud are overlain on each georeferenced image.

5. Analysis of Volcanic Ash/Dust Probabilities

An initial assessment of the naïve Bayesian method, used to identify which satellite pixels are most likely to contain volcanic ash/dust, is conducted through the analysis of four ash/dust cases captured by MODIS. Each of the four cases (two volcanic ash and two dust) is independent of the classifier training data, and the ash/dust probability is assessed within the context of human expert-estimated horizontal cloud boundaries and the traditional "split-window" technique for detecting volcanic ash and dust. Ash/dust probability

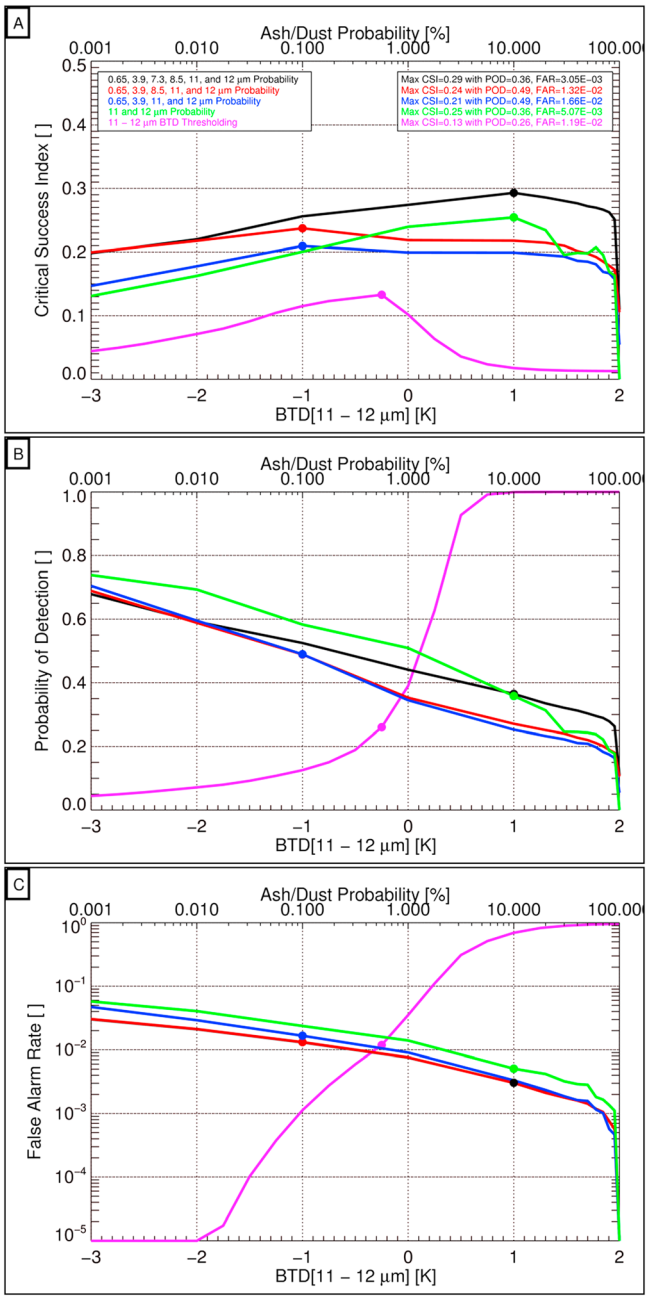

Figure 10. Skill statistics of threshold-based ash/dust detection, applied to several different metrics, are shown as a function of the selected threshold. The thresholds are relevant to the following metrics: 0.65, 3.9, 7.3, 8.5, 11, and 12 μm-based probability (black), 0.65, 3.9, 8.5, 11, and 12 μm-based probability (red), 0.65, 3.9, 11, and 12 μm-based probability (blue), 11 and 12 μm-based probability (green), and BTD (11–12 μm). The statistics are valid for a 5 min MODIS granule with a starting time of 19 February 2001 at 23:10 UTC. The bottom *x* axis is BTD (11–12 μm), and the top *x* axis is ash/dust probability. The (a) critical success index (CSI), (b) probability of detection, and (c) false alarm rate are shown. The circles denote the threshold where the CSI is a maximum.

results are generated using four different spectral channel combinations that are commonly available on operational and research satellite radiometers.

1. 0.65 (daytime only), 3.9, 7.3, 8.5, 11, and 12 μm (SC1, SC = spectral combination)
2. 0.65 (daytime only), 3.9, 8.5, 11, and 12 μm (SC2)
3. 0.65 (daytime only), 3.9, 11, and 12 μm (SC3)
4. 11 and 12 μm (SC4)

The goal of the manual analysis of the ash/dust cloud boundaries was to define a region of interest (ROI) that contains the portion of the ash/dust cloud that can be manually identified in multispectral imagery, either directly or through spatial deduction. All conclusions drawn from the comparison to the manually determined ROI are derived from relative relationships. As such, small perturbations to the ROI do not impact the results as long as ash or dust pixels that exhibit a robust spectral signature (i.e., are obvious in the imagery) are not left out of the ROI.

5.1. Volcanic Ash From Mount Cleveland (Daytime)

The ash/dust probabilities are analyzed using the previously discussed daytime scene with airborne volcanic ash (and SO_2) from an explosive eruption of Mount Cleveland, AK, that began on 19 February 2001 at approximately 14:30 UTC [*McGimsey et al.*, 2004]. The starting date and time of the *Terra* MODIS granule is 19 February 2001 at 23:10 UTC. The results, along with reference imagery, are shown in Figure 9. The bounds of the manually derived ROI are overlain on each georeferenced image in Figures 9a–9d. While the spatial distribution of the ash optical depth is unknown, the 11 μm brightness temperature image (Figure 9c) indicates that much of the cloud is quite tenuous (has a small optical depth). The ash/dust probability image (the transition from red to orange in the color bar indicates a transition to probabilities that are less than 10%) and the normalized histogram of ash/dust probability (inside and outside of the ROI) are shown for SC1. Recall that probabilities are only computed for pixels that passed the prescreening tests described

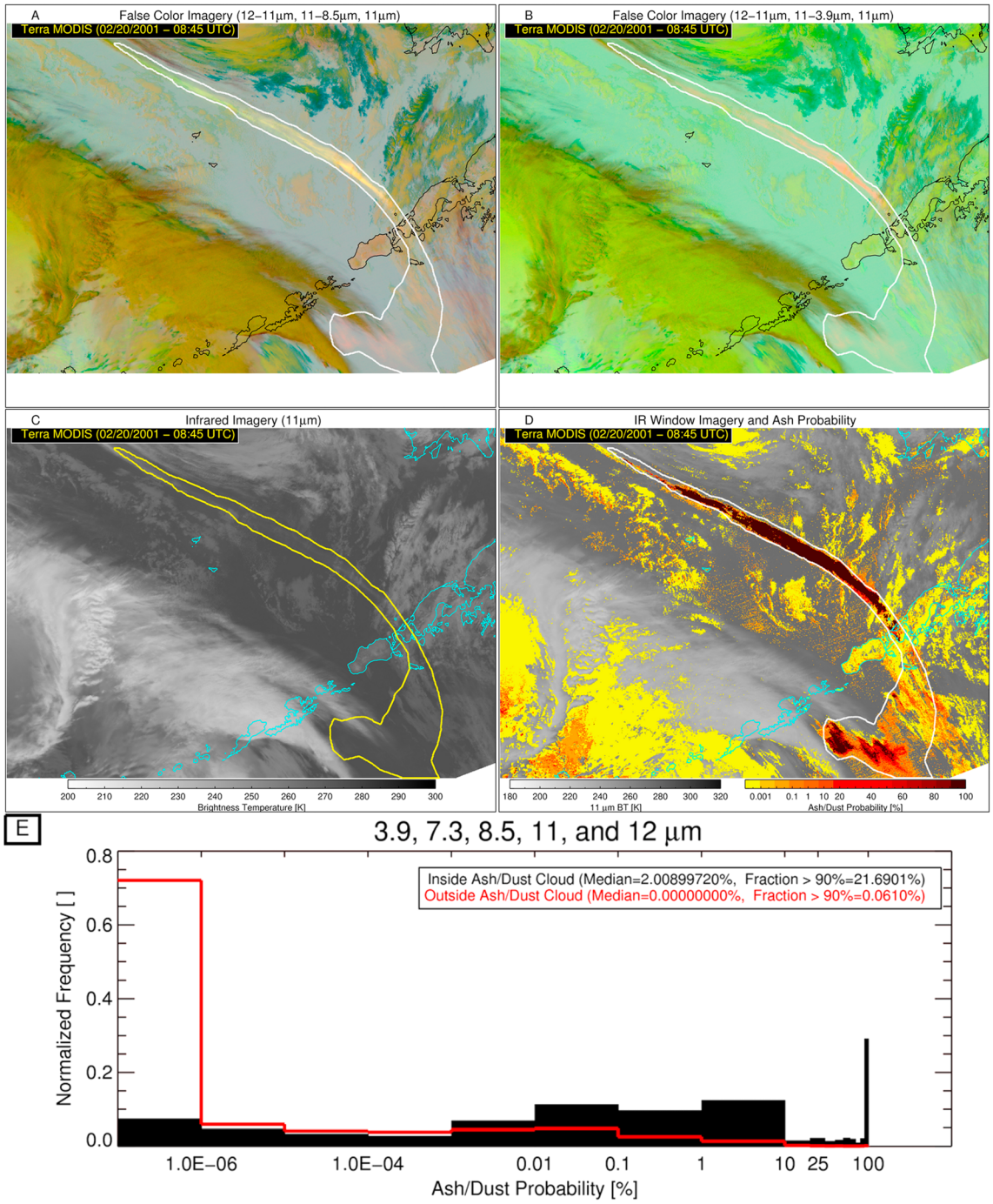

Figure 11. Same as Figure 9 except for a *Terra* MODIS image from 20 February 2001 at 08:45 UTC. Since this is a nighttime scene, the 0.65 μm channel is not utilized.

earlier. The 11 μm brightness temperature is shown in the geolocated images wherever the pixel probability is not computed. The histograms were created using the entire 5 min MODIS granule, not just the subgranule region shown in the georeferenced images (for the sake of clarity) within Figure 9. The ash/dust probability is expressed as a percentage, and log scaling is used in to enhance details at low probabilities.

While only the SC1 results are shown, every channel combination tested demonstrates that the Bayesian method has good skill, as the amount of overlap between pixels inside and outside the ROI is relatively small but does increase as the number of spectral channels utilized decreases, as one would expect if the spectral channels that are removed add value. Additional analysis was conducted to better quantify

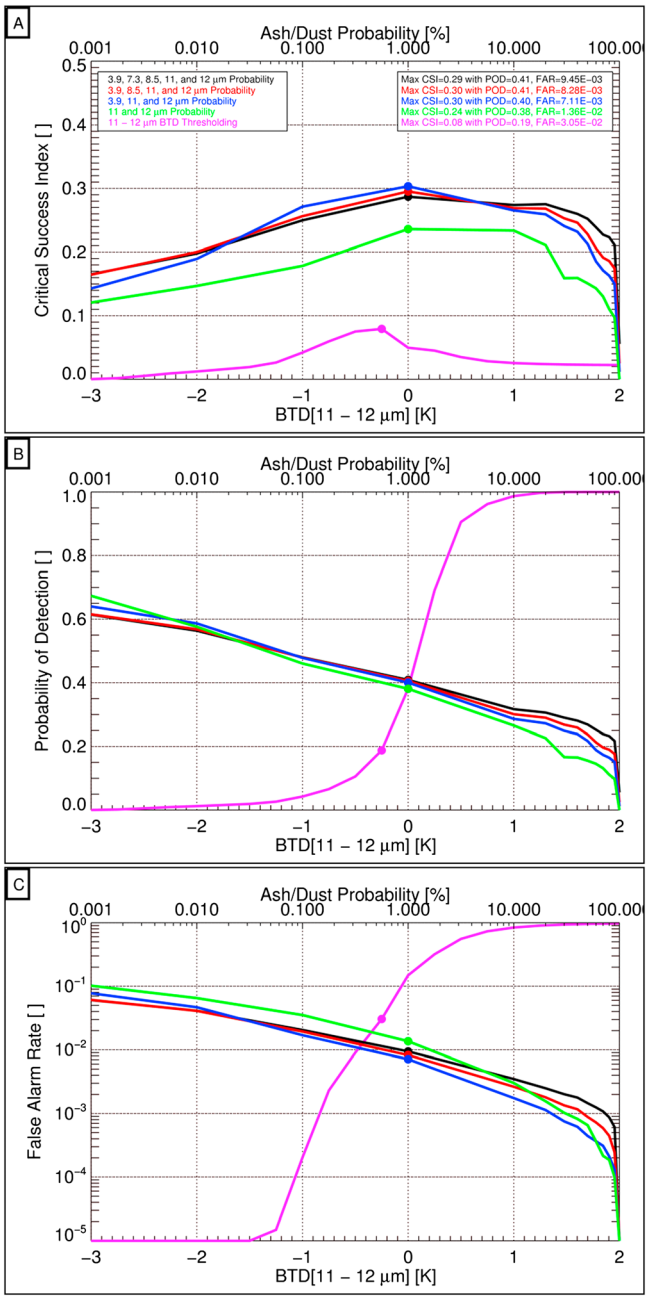

Figure 12. Same as Figure 10 except the statistics are valid for a 5 min *Terra* MODIS granule with a starting time of 20 February 2001 at 08:45 UTC.

theperformance of each spectral channel combination relative to the traditional "split-window" BTD. Performance-related statistics (Figure 10a: CSI, Figure 10b: POD, and Figure 10c: FAR) are shown in Figure 10. The statistics are shown as a function of the threshold used to create a binary yes/no ash/dust mask from the probability derived from each spectral channel combination as well as the "split-window" BTD. The simple binary masks are not the end goal; it is just used to assess the performance of the Bayesian method by quantifying the amount of overlap between the ash/dust and nonash/nondust classes. The ash/dust probability threshold is shown on the top *x* axis of Figure 10, and the 11–12 μm BTD threshold is shown on the bottom *x* axis. The SC1, SC2, SC3, SC4, and "split-window" BTD results are shown in black, red, blue, green, and magenta, respectively. The filled colored circles indicate which threshold, used to create a binary mask, produces the largest CSI. The ash/dust probability metric always produces a significantly larger maximum CSI than the "split-window" BTD. More specifically, SC1 produces the greatest maximum CSI (0.29), followed by SC4 (0.25), SC2 (0.24), SC3 (0.21), and the "split-window" BTD (0.13). The ranking of SC4 slightly ahead of SC2 and SC3 indicates that β_{tot}(7.3 μm, 11 μm) is adding good value in this case, primarily due to the presence of SO_2, and the ρ(3.9 μm, 0.65 μm) signal in certain portions of the cloud is weak ($<$0.3) as shown in Figure 4i. The weak ρ(3.9 μm, 0.65 μm) signals are collocated with regions where the cloud is hardly identifiable in 11 μm imagery, indicative of very low optical depths, where a strong ρ(3.9 μm, 0.65 μm) signal is not expected [*Pavolonis et al.*, 2006]. Finally, even though the same two spectral channels (11 and 12 μm) are used, SC4 is much more skillful at distinguishing ash/dust from all other features than the 11–12 μm BTD alone, which illustrates the power of using ε_{tot}(11 μm) and β ratios in lieu of, or in addition to, BTDs.

5.2. Volcanic Ash From Mount Cleveland (Nighttime)

In the 9.5 h between *Terra* MODIS overpasses, volcanic ash and gases from the explosive 19 February 2001 eruption of Cleveland dispersed along a NW/SE axis and were advected northeastward by the atmospheric winds. Results from the 20 February 2001 08:45 UTC *Terra* MODIS (nighttime) overpass are shown in Figure 11. The 11 μm brightness temperature image (Figure 11c) indicates that nearly the entire ash cloud

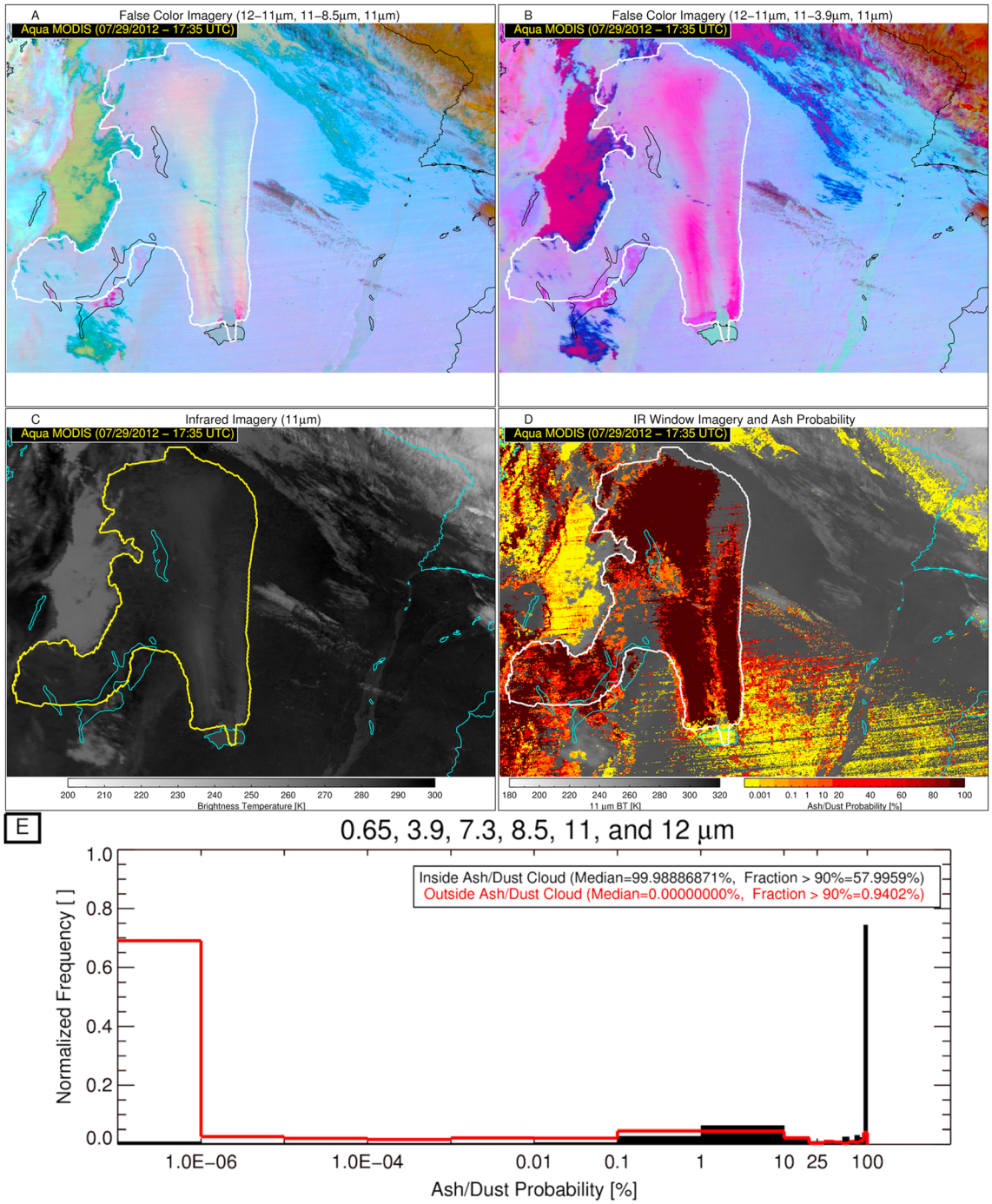

Figure 13. Same as Figure 9 except for an *Aqua* MODIS image from 29 July 2012 at 17:35 UTC.

is now highly semitransparent to infrared radiation and quite difficult to see in single-channel infrared imagery, more so than in the 19 February 2001 23:10 UTC *Terra* MODIS overpass shown earlier, likely due to dispersion and ash fallout processes. Similar to the 19 February Cleveland volcanic ash example, the overlap in the ash/dust probability distribution inside and outside of the ROI is rather small but does increase when less spectral channels are utilized. Performance metrics analogous to Figure 10 are shown in Figure 12. Once again, the ash/dust probability metric always produces a significantly larger maximum CSI than the "split-window" BTD maximum value of 0.08. SC1, SC2, and SC3 produce maximum CSI of about 0.30, while SC4 has a maximum CSI of 0.24. The SC4 maximum CSI of 0.24 is three times greater than

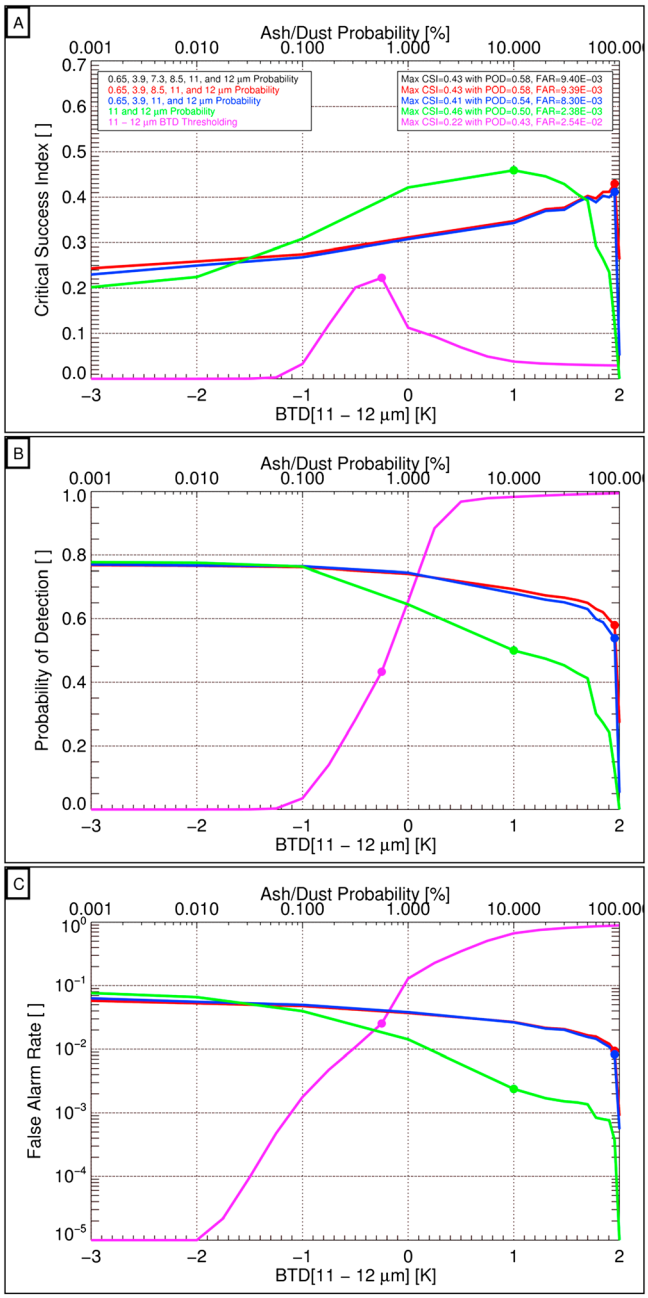

Figure 14. Same as Figure 10 except the statistics are valid for a 5 min *Aqua* MODIS granule with a starting time of 29 July 2012 at 17:35 UTC.

the "split-window" maximum of 0.08, further illustrating the value of using $\varepsilon_{tot}(11\,\mu m)$ and β ratios. Even though the CSI analysis indicates that additional spectral channels do not always have a large impact, it will be shown in Part 2 of this paper [*Pavolonis et al.*, 2015] that the extra spectral channels do have noticeable positive impact on the final results of the complete SECO algorithm.

5.3. South American Dust (Daytime)

The Bayesian method was also applied to a dust case where sediments, primarily composed of gypsum, calcite, and halite [*Piovano et al.*, 2002; *Varandas da Silva et al.*, 2008], from dried up portions of Laguna Mar Chiquita, a saline lake in central Argentina, were lofted into the atmosphere by strong winds on 29 July 2012 (a small portion of the dust area may be the result of secondary sources). Not only is this case independent of the training data set, the training data set also did not include any South American dust cases, let alone a case with a unique rock type that is associated with a relatively localized source. In addition, the dust is primarily located over land, where uncertainty in the clear-sky radiance calculations is greater compared to water surfaces. Thus, this case is quite useful for demonstrating the robustness of the Bayesian method. The starting date and time of the *Aqua* MODIS granule used in this analysis is 29 July 2012 at 17:35 UTC (daytime). The results are shown in Figures 13 and 14. Because of its relatively unique composition, the dust does not take on the typical reddish color in the 12–11 μm, 11–8.5 μm, and 11 μm false color image (Figure 13a). The manually analyzed bounds of the dust cloud were primarily determined from the 12–11 μm, 11–3.9 μm, and 11 μm false color image (Figure 13b) where the cloud is more readily apparent. The dust cloud ROI is also consistent with MODIS true color imagery (https://earthdata.nasa.gov/labs/worldview/). While the ash/dust probability within the dust cloud is generally quite large (>80%), a fair number of larger values are also found outside of the ROI compared to the over-water Cleveland volcanic ash cases. The larger probabilities outside of the ROI are mainly caused by spectral variability in surface emissivity that resembles ash/dust clouds, coupled with errors in the clear-sky radiance calculations (largely driven by errors in land surface temperature). Nevertheless, the overlap in ash/dust probability inside and outside of the ROI is quite small and increases when fewer spectral channels are used, as indicated by the statistics shown in Figure 14. The maximum CSI associated with applying

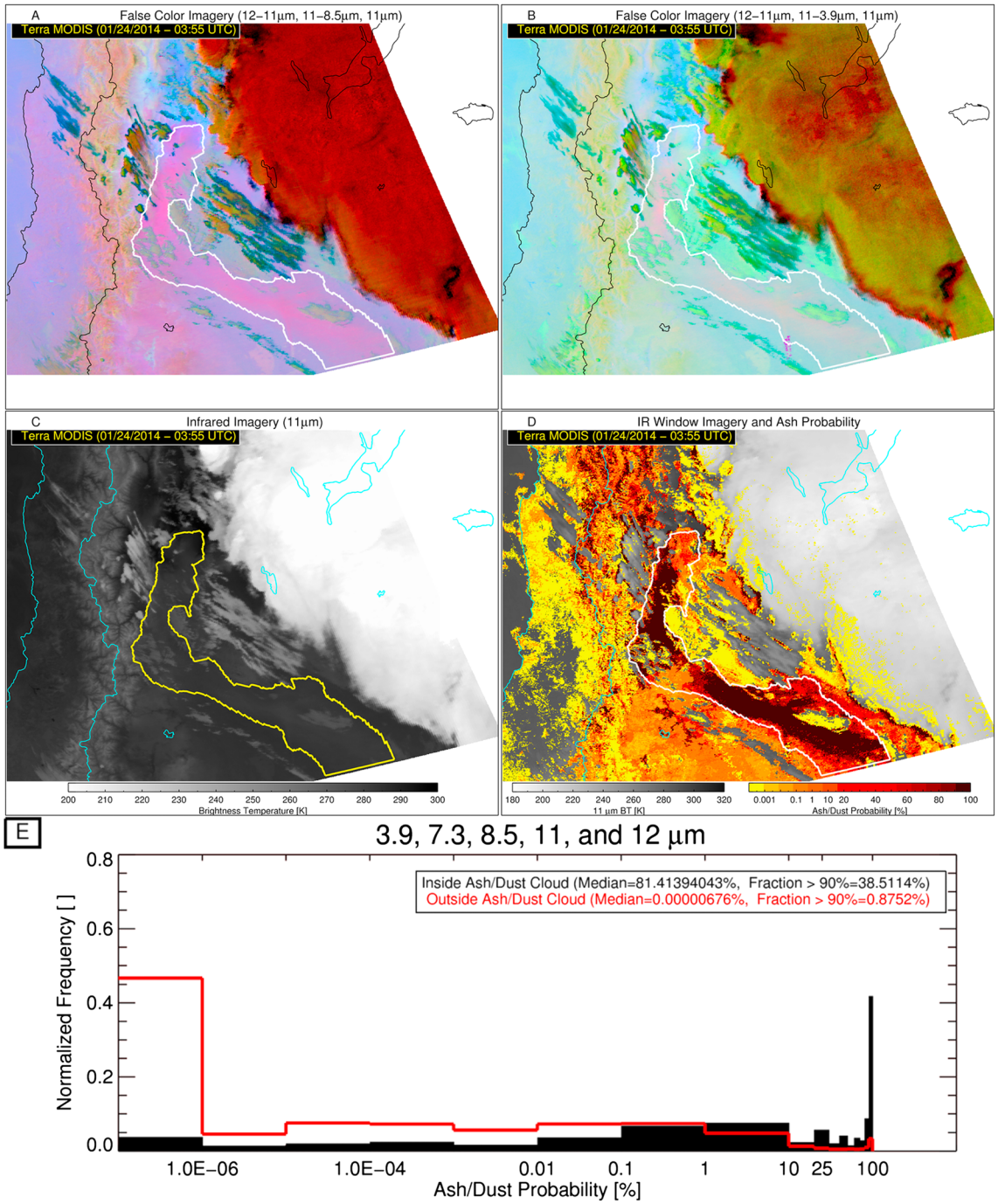

Figure 15. Same as Figure 9 except for a *Terra* MODIS image from 24 January 2014 at 03:55 UTC. Since this is a nighttime scene, the 0.65 μm channel is not utilized.

a threshold to the ash/dust probability (0.43, 0.43, 0.41, and 0.46 for SC1, SC2, SC3, and SC4, respectively) is still nearly twice the maximum CSI that can be achieved by applying a threshold to the "split-window" BTD (0.22) for this MODIS granule (Figure 14), regardless of the spectral channel combination used in estimating ash/dust probability. Despite the complexities introduced by a variety of complicated land surface types, the FAR associated with the maximum ash/dust CSI is comparable to the over-ocean Cleveland ash scenes, but the probability threshold required to achieve the maximum CSI does vary quite a bit from scene to scene. This issue is addressed in Part 2 of this paper [*Pavolonis et al.,* 2015].

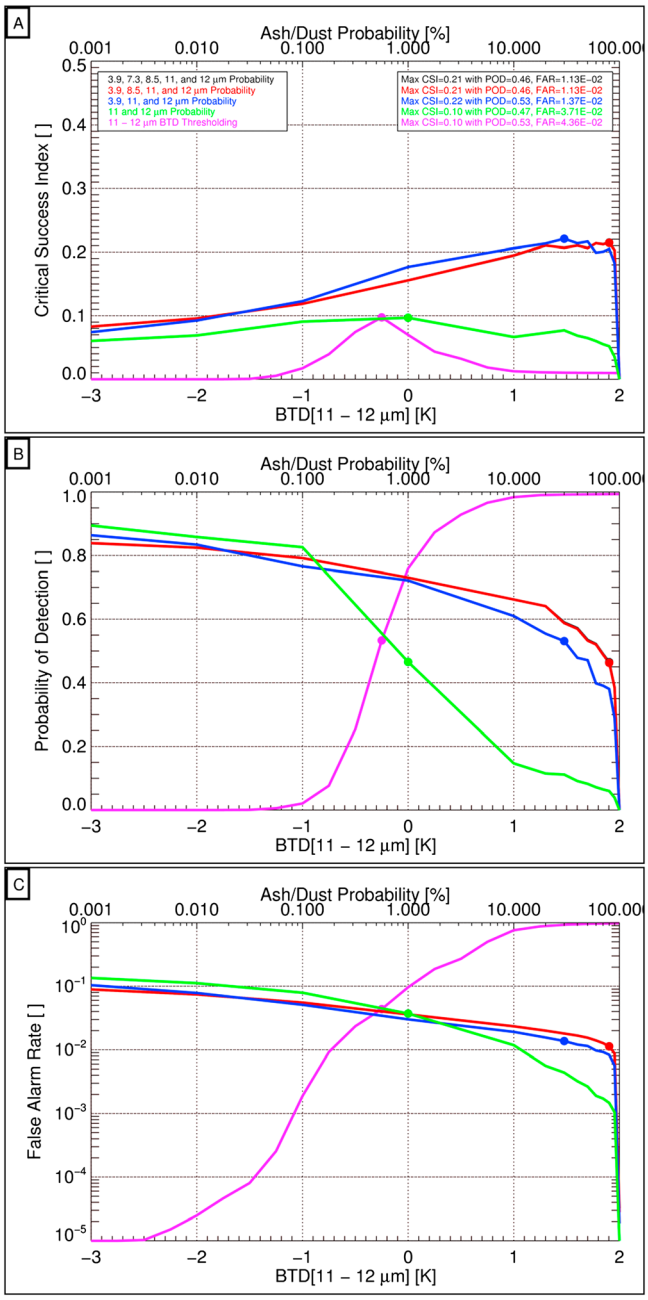

Figure 16. Same as Figure 10 except the statistics are valid for a 5 min *Terra* MODIS granule with a starting time of 24 January 2014 at 03:55 UTC.

5.4. South American Dust (Nighttime)

Dust lofted from the western portion of the Argentinean Pampa (plain) by a nocturnal thunderstorm outflow boundary on 24 January 2014 was also examined. Feldspars and quartz tend to be the primary mineral components of dust that originates from the Argentinean Pampa [*Ramsperger et al.*, 1998a, 1998b]. The starting date and time of the *Terra* MODIS granule used in this analysis is 24 January 2014 at 03:55 UTC, and the results are shown in Figures 15 and 16. Similar to the Laguna Mar Chiquita dust scene, pixels outside of the manually derived ROI sometimes have a larger probability due to surface emissivity effects and errors in the clear-sky radiative transfer (Figure 15). In addition, unlike the previous three cases, the SC4-derived ash/dust probabilities are not particularly skillful in this over-land nighttime scene, likely as a result of less contrast between the temperature of the dust cloud and the background. The additional spectral information offered by SC1, SC2, and SC3 adds more value in the low-temperature contrast situations commonly encountered at night. As shown in Figure 16, the maximum CSI of the SC1- (0.21), SC2- (0.21), and SC3-derived (0.22) ash/dust probabilities is more than twice the maximum CSI of the "split-window" BTD (0.10). The maximum CSI of SC4 does not improve upon the "split-window" BTD likely due to low signal to noise and clear-sky radiative transfer errors. Overall, the Bayesian method has been demonstrated to be skillful in distinguishing ash/dust and nonash/nondust features, day and night, over land and over water. Pixel and cloud object filters that minimize the impact of clear-sky radiative transfer errors, like those encountered in the two South American dust scenes, are described by *Pavolonis et al.* [2015].

6. Conclusions

The SECO volcanic ash and dust detection algorithm, which can be applied to nearly any satellite sensor at all times of the day, consists of four major components. The first two components, computation of advanced radiative metrics and estimation of the probability that a given pixel contains volcanic ash and/or dust, were described in this paper. The remaining two parts, construction of cloud objects and the selection of volcanic ash/dust cloud objects, are described in a companion paper [*Pavolonis et al.*, 2015]. The methodology for

computing advanced radiative metrics, such as effective absorption optical depth ratios (β ratios), was described. Multispectral infrared measurements are expressed as β ratios, as opposed to traditional brightness temperature differences (BTDs), because β ratios provide increased sensitivity to cloud microphysical properties, including cloud composition. A naïve Bayesian approach was developed to take advantage of the volcanic ash/dust-relevant cloud composition information that the β ratios provide. Various empirically derived multivariate classifiers were constructed by coupling β ratios, computed from the radiance measured at approximately 11 and 12 μm, with visible and near-infrared measurements (0.65 and/or 3.9 μm) or β ratios that are computed using other spectral channel pairs (8.5/11 μm and 7.3/11 μm). Several case studies showed that the naïve Bayesian approach is quite skillful even when only subsets of the allowable spectral channels are utilized. The skill of the Bayesian approach was also shown to greatly exceed the traditional "split-window" method used to detect volcanic ash and dust.

The ultimate objective of the automated SECO approach is to produce a binary volcanic ash/dust mask that is comparable in skill to a mask that is manually constructed by a human expert. Discrimination of ash and dust is important and will be the focus of future SECO development efforts. Despite the success of the Bayesian method, it, alone, is not skillful enough to construct a human expert-like binary mask by simply applying a probability threshold. As shown by *Pavolonis et al.* [2015], the Bayesian method must be combined with advanced spatial analysis techniques to produce such a result.

Acknowledgments
NOAA GOES-R Risk Reduction funded this research. The MODIS data utilized in this study are freely available from the NASA Level 1 and Atmosphere Archive and Distribution System (LAADS) at http://ladsweb.nascom.nasa.gov/. The software utilized to generate the results described in this paper is available upon request by sending an email to Mike.Pavolonis@noaa.gov. We thank Dr. Fred Prata and an anonymous reviewer for helping improve the quality of the manuscript. The views, opinions, and findings contained in this report are those of the author(s) and should not be construed as an official National Oceanic and Atmospheric Administration or U.S. Government position, policy, or decision.

References

Ackerman, S. (1997), Remote sensing aerosols using satellite infrared observations, *J. Geophys. Res.*, *102*(D14), 17,069–17,079, doi:10.1029/96JD03066.

Arason, P., G. N. Petersen, and H. Bjornsson (2011), Observations of the altitude of the volcanic plume during the eruption of Eyjafjallajokull, April–May 2010, *Earth Syst. Sci. Data*, *3*(1), 9–17, doi:10.5194/essd-3-9-2011.

Ashpole, I., and R. Washington (2012), An automated dust detection using SEVIRI: A multiyear climatology of summertime dustiness in the central and western Sahara, *J. Geophys. Res.*, *117*, D08202, doi:10.1029/2011JD016845.

Casadevall, T. (1994), The 1989–1990 eruption of redoubt volcano, Alaska—Impacts on aircraft operations, *J. Volcanol. Geotherm. Res.*, *62*(1–4), 301–316, doi:10.1016/0377-0273(94)90038-8.

Cintineo, J. L., M. J. Pavolonis, J. M. Sieglaff, and D. T. Lindsey (2014), An empirical model for assessing the severe weather potential of developing convection, *Weather Forecasting*, *29*, 639–653, doi:10.1175/waf-d-13-00113.1.

Clarisse, L., F. Prata, J. Lacour, D. Hurtmans, C. Clerbaux, and P. Coheur (2010), A correlation method for volcanic ash detection using hyperspectral infrared measurements, *Geophys. Res. Lett.*, *37*, L19806, doi:10.1029/2010GL044828.

Clarisse, L., P. Coheur, F. Prata, J. Hadji-Lazaro, D. Hurtmans, and C. Clerbaux (2013), A unified approach to infrared aerosol remote sensing and type specification, *Atmos. Chem. Phys.*, *13*(4), 2195–2221, doi:10.5194/acp-13-2195-2013.

Corradini, S., L. Merucci, A. Prata, and A. Piscini (2010), Volcanic ash and SO_2 in the 2008 Kasatochi eruption: Retrievals comparison from different IR satellite sensors, *J. Geophys. Res.*, *115*, D00L21, doi:10.1029/2009JD013634.

Cox, S. K. (1976), Observations of cloud infrared effective emissivity, *J. Atmos. Sci.*, *33*(2), 287–289, doi:10.1175/1520-0469(1976)033<0287:oociee>2.0.co;2.

Darmenov, A., and I. Sokolik (2005), Identifying the regional thermal-IR radiative signature of mineral dust with MODIS, *Geophys. Res. Lett.*, *32*, L16803, doi:10.1029/2005GL023092.

de Graaf, M., P. Stammes, O. Torres, and R. Koelemeijer (2005), Absorbing Aerosol Index: Sensitivity analysis, application to GOME and comparison with TOMS, *J. Geophys. Res.*, *110*, D01201, doi:10.1029/2004JD005178.

DeSouza-Machado, S., et al. (2010), Infrared retrievals of dust using AIRS: Comparisons of optical depths and heights derived for a North African dust storm to other collocated EOS A-Train and surface observations, *J. Geophys. Res.*, *115*, D15201, doi:10.1029/2009JD012842.

Diner, D. J., et al. (2001), MISR aerosol optical depth retrievals over southern Africa during the SAFARI-2000 dry season campaign, *Geophys. Res. Lett.*, *28*(16), 3127–3130, doi:10.1029/2001GL013188.

Domingos, P., and M. Pazzani (1997), On the optimality of the simple Bayesian classifier under zero-one loss, *Mach. Learn.*, *29*(2–3), 103–130, doi:10.1023/a:1007413511361.

Dunion, J., and C. Velden (2004), The impact of the Saharan air layer on Atlantic tropical cyclone activity, *Bull. Am. Meteorol. Soc.*, *85*(3), 353, doi:10.1175/BAMS-85-3-353.

Ellrod, G., B. Connell, and D. Hillger (2003), Improved detection of airborne volcanic ash using multispectral infrared satellite data, *J. Geophys. Res.*, *108*(D12), 4356, doi:10.1029/2002JD002802.

Ellrod, G. P. (2004), Impact on volcanic ash detection caused by the loss of the 12.0 μm "split window" band on GOES imagers, *J. Volcanol. Geotherm. Res.*, *135*(1–2), 91–103, doi:10.1016/j.jvolgeores.2003.12.009.

Evan, A., A. Heidinger, and M. Pavolonis (2006), Development of a new over-water advanced very high resolution radiometer dust detection algorithm, *Int. J. Remote Sens.*, *27*(18), 3903–3924, doi:10.1080/01431160600646359.

Evan, A., G. Foltz, D. Zhang, and D. Vimont (2011), Influence of African dust on ocean-atmosphere variability in the tropical Atlantic, *Nat. Geosci.*, *4*(11), 762–765, doi:10.1038/NGEO1276.

Francis, P., M. Cooke, and R. Saunders (2012), Retrieval of physical properties of volcanic ash using Meteosat: A case study from the 2010 Eyjafjallajokull eruption, *J. Geophys. Res.*, *117*, D00U09, doi:10.1029/2011JD016788.

Gangale, G., A. Prata, and L. Clarisse (2010), The infrared spectral signature of volcanic ash determined from high-spectral resolution satellite measurements, *Remote Sens. Environ.*, *114*(2), 414–425, doi:10.1016/j.rse.2009.09.007.

Giraud, V., J. C. Buriez, Y. Fouquart, F. Parol, and G. Seze (1997), Large-scale analysis of cirrus clouds from AVHRR data: Assessment of both a microphysical index and the cloud-top temperature, *J. Appl. Meteorol.*, *36*(6), 664–675, doi:10.1175/1520-0450-36.6.664.

Guffanti, M., D. Schneider, K. Wallace, T. Hall, D. Bensimon, and L. Salinas (2010), Aviation response to a widely dispersed volcanic ash and gas cloud from the August 2008 eruption of Kasatochi, Alaska, USA, *J. Geophys. Res.*, *115*, D00L19, doi:10.1029/2010JD013868.

Hadley, D., G. L. Hufford, and J. J. Simpson (2004), Resuspension of relic volcanic ash and dust from Katmai: Still an aviation hazard, *Weather Forecasting*, *19*(5), 829–840, doi:10.1175/1520-0434(2004)019<0829:rorvaa>2.0.co;2.

Hamill, T. M., J. S. Whitaker, and S. L. Mullen (2006), Reforecasts—An important dataset for improving weather predictions, *Bull. Am. Meteorol. Soc.*, *87*(1), 33, doi:10.1175/bams-87-1-33.

Hand, D. J., and K. M. Yu (2001), Idiot's Bayes—Not so stupid after all?, *Int. Stat. Rev.*, *69*(3), 385–398, doi:10.2307/1403452.

Hannon, S., L. L. Strow, and W. W. McMillan (1996), Atmospheric infrared fast transmittance models: A comparison of two approaches, paper presented at Conference on Optical Spectroscopic Techniques and Instrumentation for Atmospheric and Space Research II, SPIE—Int. Soc. Opt. Eng., Denver, Colo.

Heidinger, A. K., A. T. Evan, M. J. Foster, and A. Walther (2012), A naive Bayesian cloud-detection scheme derived from CALIPSO and applied within PATMOS-x, *J. Appl. Meteorol. Climatol.*, *51*(6), 1129–1144, doi:10.1175/jamc-d-11-02.1.

Heidinger, A., and M. Pavolonis (2009), Gazing at cirrus clouds for 25 years through a split window. Part I: Methodology, *J. Appl. Meteorol. Climatol.*, *48*(6), 1100–1116, doi:10.1175/2008JAMC1882.1.

Heidinger, A., M. Pavolonis, R. Holz, B. Baum, and S. Berthier (2010), Using CALIPSO to explore the sensitivity to cirrus height in the infrared observations from NPOESS/VIIRS and GOES-R/ABI, *J. Geophys. Res.*, *115*, D00H20, doi:10.1029/2009JD012152.

Hillger, D., and J. Clark (2002a), Principal component image analysis of MODIS for volcanic ash. Part I: Most important bands and implications for future GOES Imagers, *J. Appl. Meteorol.*, *41*(10), 985–1001.

Hillger, D., and J. Clark (2002b), Principal component image analysis of MODIS for volcanic ash. Part II: Simulation of current GOES and GOES-M imagers, *J. Appl. Meteorol.*, *41*(10), 1003–1010, doi:10.1175/1520-0450(2002)041<1003:PCIAOM>2.0.CO;2.

Hong, S. (2009), Detection of Asian dust (Hwangsa) over the Yellow Sea by decomposition of unpolarized infrared reflectivity, *Atmos. Environ.*, *43*(37), 5887–5893, doi:10.1016/j.atmosenv.2009.08.024.

Hsu, N. C., M. J. Jeong, C. Bettenhausen, A. M. Sayer, R. Hansell, C. S. Seftor, J. Huang, and S. C. Tsay (2013), Enhanced Deep Blue aerosol retrieval algorithm: The second generation, *J. Geophys. Res. Atmos.*, *118*, 9296–9315, doi:10.1002/jgrd.50712.

ICAO (2007), Manual on volcanic ash, radioactive material, and toxic chemical clouds, *Rep.*, 500 pp. [Available at http://www.paris.icao.int/news/pdf/9691.pdf.]

Inoue, T. (1985), On the temperature and effective emissivity determination of semi-transparent cirrus clouds by bi-spectral measurements in the 10 mu-m window region, *J. Meteorol. Soc. Jpn.*, *63*(1), 88–99.

Inoue, T. (1987), A cloud type classification with NOAA 7 split-window measurements, *J. Geophys. Res.*, *92*(D4), 3991–4000, doi:10.1029/JD092iD04p03991.

Jickells, T., et al. (2005), Global iron connections between desert dust, ocean biogeochemistry, and climate, *Science*, *308*(5718), 67–71, doi:10.1126/science.1105959.

Kossin, J. P., and M. Sitkowski (2009), An objective model for identifying secondary eyewall formation in hurricanes, *Mon. Weather Rev.*, *137*(3), 876–892, doi:10.1175/2008mwr2701.1.

Legrand, M., A. Plana-Fattori, and C. N'doume (2001), Satellite detection of dust using the IR imagery of Meteosat 1. Infrared difference dust index, *J. Geophys. Res.*, *106*(D16), 18,251–18,274, doi:10.1029/2000JD900749.

Lensky, I., and D. Rosenfeld (2008), Clouds-Aerosols-Precipitation Satellite Analysis Tool (CAPSAT), *Atmos. Chem. Phys.*, *8*(22), 6739–6753.

Liu, D., Z. Wang, Z. Liu, D. Winker, and C. Trepte (2008), A height resolved global view of dust aerosols from the first year CALIPSO lidar measurements, *J. Geophys. Res.*, *113*, D16214, doi:10.1029/2007JD009776.

Mackie, S., and M. Watson (2014), Probabilistic detection of volcanic ash using a Bayesian approach, edited, *J. Geophys. Res. Atmos*, *119*, 2409–2428, doi:10.1002/2013JD021077.

McGimsey, R. G., C. A. Neal, and O. Girina (2004), 2001 volcanic activity in Alaska and Kamchatka: Summary of events and response of the Alaska Volcano Observatory, *Rep.*, 53 pp., U.S. Geol. Surv.

Merchant, C. J., A. R. Harris, E. Maturi, and S. MacCallum (2005), Probabilistic physically based cloud screening of satellite infrared imagery for operational sea surface temperature retrieval, *Q. J. R. Meteorol. Soc.*, *131*(611), 2735–2755, doi:10.1256/qj.05.15.

Miller, S. (2003), A consolidated technique for enhancing desert dust storms with MODIS, *Geophys. Res. Lett.*, *30*(20), 2071, doi:10.1029/2003GL018279.

Miller, T. P., and T. J. Casadevall (2000), Volcanic ash hazards to aviation, in *Encyclopedia of Volcanoes*, edited by H. Sigurdsson, pp. 915–930, Academic, San Diego, Calif.

Millington, S., R. Saunders, P. Francis, and H. Webster (2012), Simulated volcanic ash imagery: A method to compare NAME ash concentration forecasts with SEVIRI imagery for the Eyjafjallajokull eruption in 2010, *J. Geophys. Res.*, *117*, D00U26, doi:10.1029/2011JD016770.

Nolin, A. W., R. Armstrong, and J. Maslanik (1998), *Near-Real-Time SSM/I-SSMIS EASE-Grid Daily Global Ice Concentration and Snow Extent*, Natl. Snow and Ice Data Cent., Boulder, Colo.

Parol, F., J. C. Buriez, G. Brogniez, and Y. Fouquart (1991), Information-content of AVHRR channels 4 and 5 with respect to the effective radius of cirrus cloud particles, *J. Appl. Meteorol.*, *30*(7), 973–984, doi:10.1175/1520-0450-30.7.973.

Pavolonis, M. (2010), Advances in extracting cloud composition information from spaceborne infrared radiances—A robust alternative to brightness temperatures. Part I: Theory, *J. Appl. Meteorol. Climatol.*, *49*(9), 1992–2012, doi:10.1175/2010JAMC2433.1.

Pavolonis, M., W. Feltz, A. Heidinger, and G. Gallina (2006), A daytime complement to the reverse absorption technique for improved automated detection of volcanic ash, *J. Atmos. Oceanic Technol.*, *23*(11), 1422–1444, doi:10.1175/JTECH1926.1.

Pavolonis, M., A. Heidinger, and J. Sieglaff (2013), Automated retrievals of volcanic ash and dust cloud properties from upwelling infrared measurements, *J. Geophys. Res. Atmos.*, *118*, 1436–1458, doi:10.1002/jgrd.50173.

Pavolonis, M. J. (2014), Development of satellite remote sensing techniques for quantifying volcanic ash cloud properties, PhD dissertation, Univ. of Wisconsin-Madison, Madison, Wis., 279 pp. [Available to http://depot.library.wisc.edu.ezproxy.library.wisc.edu/repository/fedora/1711.dl:7M4TFYMUM5Z5Z8N/datastreams/REF/content.]

Pavolonis, M. J., J. Sieglaff, and J. Cintineo (2015), Spectrally Enhanced Cloud Objects—A generalized framework for automated detection of volcanic ash and dust clouds using passive satellite measurements: 2. Cloud object analysis and global application, *J. Geophys. Res. Atmos.*, *120*, doi:10.1002/2014JD022969.

Peyridieu, S., et al. (2013), Characterisation of dust aerosols in the infrared from IASI and comparison with PARASOL, MODIS, MISR, CALIOP, and AERONET observations, *Atmos. Chem. Phys.*, *13*(12), 6065–6082, doi:10.5194/acp-13-6065-2013.

Piovano, E. L., D. Ariztegui, and S. D. Moreira (2002), Recent environmental changes in Laguna Mar Chiquita (central Argentina): A sedimentary model for a highly variable saline lake, *Sedimentology*, *49*(6), 1371–1384, doi:10.1046/j.1365-3091.2002.00503.x.

Prata, A. (1989a), Infrared radiative-transfer calculations for volcanic ash clouds, *Geophys. Res. Lett.*, *16*(11), 1293–1296, doi:10.1029/GL016i011p01293.

Prata, A. (1989b), Observations of volcanic ash clouds in the 10–12-mu-m window using AVHRR/2 data, *Int. J. Remote Sens.*, *10*(4–5), 751–761.
Prata, A., and I. Grant (2001), Retrieval of microphysical and morphological properties of volcanic ash plumes from satellite data: Application to Mt Ruapehu, New Zealand, *Q. J. R. Meteorol. Soc.*, *127*(576), 2153–2179, doi:10.1256/smsqj.57614.
Prata, A., and A. Prata (2012), Eyjafjallajokull volcanic ash concentrations determined using spin enhanced visible and infrared imager measurements, *J. Geophys. Res.*, *117*, D00U23, doi:10.1029/2011JD016800.
Prospero, J., and P. Lamb (2003), African droughts and dust transport to the Caribbean: Climate change implications, *Science*, *302*(5647), 1024–1027, doi:10.1126/science.1089915.
Ramsay, B. H. (1998), The interactive multisensor snow and ice mapping system, *Hydrol. Processes*, *12*(10–11), 1537–1546, doi:10.1002/(sici)1099-1085(199808/09)12:10/11<1537::aid-hyp679>3.0.co;2-a.
Ramsperger, B., L. Herrmann, and K. Stahr (1998a), Dust characteristics and source-sink relations in eastern west Africa (SW-Niger and Benin) and South America (Argentinean pampas), *Z. Pflanzenernahr. Bodenkd.*, *161*(4), 357–363.
Ramsperger, B., N. Peinemann, and K. Stahr (1998b), Deposition rates and characteristics of aeolian dust in the semi-arid and sub-humid regions of the Argentinean Pampa, *J. Arid Environ.*, *39*(3), 467–476, doi:10.1006/jare.1997.0366.
Remer, L. A., S. Mattoo, R. C. Levy, and L. A. Munchak (2013), MODIS 3 km aerosol product: Algorithm and global perspective, *Atmos. Meas. Tech.*, *6*(7), 1829–1844, doi:10.5194/amt-6-1829-2013.
Rose, W. I., G. J. S. Bluth, and G. G. J. Ernst (2000), Integrating retrievals of volcanic cloud characteristics from satellite remote sensors: A summary, *Philos. Trans. R. Soc. London, Ser. A*, *358*(1770), 1585–1606.
Schmit, T. J., E. M. Prins, A. J. Schreiner, and J. J. Gurka (2001), Introducing the GOES-M imager, *Nat. Weather Dig.*, *25*(34), 28–37.
Schneider, D. J., and R. P. Hoblitt (2013), Doppler weather radar observations of the 2009 eruption of Redoubt Volcano, Alaska, *J. Volcanol. Geotherm. Res.*, *259*, 133–144, doi:10.1016/j.jvolgeores.2012.11.004.
Schneider, D. J., W. I. Rose, L. R. Coke, G. J. S. Bluth, I. E. Sprod, and A. J. Krueger (1999), Early evolution of a stratospheric volcanic eruption cloud as observed with TOMS and AVHRR, *J. Geophys. Res.*, *104*(D4), 4037–4050, doi:10.1029/1998JD200073.
Scollo, S., R. Kahn, D. Nelson, M. Coltelli, D. Diner, M. Garay, and V. Realmuto (2012), MISR observations of Etna volcanic plumes, *J. Geophys. Res.*, *117*, D06210, doi:10.1029/2011JD016625.
Seemann, S. W., E. E. Borbas, R. O. Knuteson, G. R. Stephenson, and H.-L. Huang (2008), Development of a global infrared land surface emissivity database for application to clear sky sounding retrievals from multispectral satellite radiance measurements, *J. Appl. Meteorol. Climatol.*, *47*(1), 108–123, doi:10.1175/2007jamc1590.1.
Tanre, D., F. M. Breon, J. L. Deuze, O. Dubovik, F. Ducos, P. Francois, P. Goloub, M. Herman, A. Lifermann, and F. Waquet (2011), Remote sensing of aerosols by using polarized, directional and spectral measurements within the A-Train: The PARASOL mission, *Atmos. Meas. Tech.*, *4*(7), 1383–1395, doi:10.5194/amt-4-1383-2011.
Turner, D. D. (2005), Arctic mixed-phase cloud properties from AERI lidar observations: Algorithm and results from SHEBA, *J. Appl. Meteorol.*, *44*, 427–444.
Uddstrom, M. J., W. R. Gray, R. Murphy, N. A. Oien, and T. Murray (1999), A Bayesian cloud mask for sea surface temperature retrieval, *J. Atmos. Oceanic Technol.*, *16*(1), 117–132, doi:10.1175/1520-0426(1999)016<0117:abcmfs>2.0.co;2.
Varandas da Silva, L. S., E. L. Piovano, D. d. A. Azevedo, and F. R. de Aquino Neto (2008), Quantitative evaluation of sedimentary organic matter from Laguna Mar Chiquita, Argentina, *Org. Geochem.*, *39*(4), 450–464, doi:10.1016/j.orggeochem.2008.01.002.
Wang, C., S. Dong, A. Evan, G. Foltz, and S. Lee (2012), Multidecadal covariability of North Atlantic sea surface temperature, African dust, Sahel rainfall, and Atlantic hurricanes, *J. Clim.*, *25*(15), 5404–5415, doi:10.1175/JCLI-D-11-00413.1.
Watson, I. M., V. J. Realmuto, W. I. Rose, A. J. Prata, G. J. S. Bluth, Y. Gu, C. E. Bader, and T. Yu (2004), Thermal infrared remote sensing of volcanic emissions using the moderate resolution imaging spectroradiometer, *J. Volcanol. Geotherm. Res.*, *135*(1–2), 75–89, doi:10.1016/j.jvolgeores.2003.12.017.
Wen, S., and W. I. Rose (1994), Retrieval of sizes and total masses of particles in volcanic clouds using AVHRR bands 4 and 5, *J. Geophys. Res.*, *99*(D3), 5421–5431, doi:10.1029/93JD03340.
Winker, D., Z. Liu, A. Omar, J. Tackett, and D. Fairlie (2012), CALIOP observations of the transport of ash from the Eyjafjallajokull volcano in April 2010, *J. Geophys. Res.*, *117*, D00U15, doi:10.1029/2011JD016499.